Investigation of blade flexibility effects over the loads and wake of a 15 MW wind turbine using a flexible actuator line method

Reply to reviewer 2

F. Trigaux, P. Chatelain, and G. Winckelmans

May 2024

We first would like to thank the reviewer for the insightful comments. All these comments have been addressed. The detailed reply is presented hereunder, as well as the suggested changes to the manuscript. The reviewer can also refer to the updated version of the manuscript, where all the changes are highlighted.

"Investigation of blade flexibility effects over the loads and wake of a 15 MW wind turbine using a flexible actuator line method" investigates the effects of blade flexibility on the forces and wakes of the IEA 15-MW wind turbine, using a LES simulation with the actuator line method (ALM) coupled with a blade structural dynamics solver. Three models for the turbine are considered: rigid undeformed blades, rigid deformed blades and flexible blades. For the case with uniform inflow, with and without turbulence, the results are compared to the results of a BEM (blade-element momentum theory) model and a free vortex wake method. The turbine is also simulated in a neutral atmospheric boundary layer.

The detailed analysis of this work includes the analysis of the distribution of forces and displacements using different methods and flexibility models, in time and frequency domains, in addition to characteristics of the wake. It is a clear contribution to the field of research and within the scope of the journal. The manuscript is well-written, with clear objectives. The results are original, with associated discussions of high scientific relevance. There are a few remarks that should be addressed before publication, please see below.

Reply Thank you for your appreciation. We have addressed the comments, and the detailed reply is provided hereunder.

Comment 1 In lines 93 and 465: reference to "advanced" ALM. However, this concept of "advanced ALM" is ill-defined. For example, previous works (Churchfield et al., 2017) have defined it by a collection of developments, however, not all of these developments seem to be implemented in the present work. Also, "advanced" may be interpreted as a common adjective, because it is not capitalized. In that sense, the concept of "advanced ALM" is questionable in the present context. For these reasons, I suggest that the term "advanced" be avoided.

Reply The term "advanced" is removed from the manuscript.

Comment 2 In line 107: The mentioned corrections are not simple tip corrections, a more modern term is "smearing corrections", because they correct for the smearing of the forces, not only at the tip. If you prefer to be more specific to this class of smearing corrections based on vortices, one usual term is "vortex-based smearing corrections".

Reply The term "tip correction" is changed to "vortex-based smearing corrections", as suggested, to avoid the confusion with tip corrections developed for the BEM or for the actuator disk method.

Comment 3 In line 111: The use of "much" in "much decreasing the need for a tip correction" might be misleading. It decreases the need for a correction, but not by orders of magnitude. Despite having a lower error than a 3D Gaussian, Caprace et al. (2019) showed that there is still a relevant error if using the 2D Gaussian without any correction.

Reply We agree that even using a 2D Gaussian mollification, the accuracy of the ALM remains problematic in the near tip region. It is however significantly better than that of the ALM with 3D Gaussian mollification (e.g., Mikkelsen (2004); Jha and Schmitz (2018); Caprace et al. (2019)). Nevertheless, "much decreasing" was modified to "decreasing".

Comment 4 In line 181: A wake length of 10 rotations without a far wake model might be too short. Please show that this choice of parameters does not have an effect on the distribution of forces (results of table 1 and figure 4).

Reply The choice of 600 panels is based on the OLAF model currently provided in the repository for the IEA-15 MW [1]. This model suggests the use of 600 near wake panels, without far wake. Yet, we agree with the reviewer that 10 rotations is the minimal wake length suggested in the guidelines, and a verification of the impact of this parameter is therefore necessary.

The OLAF simulations are thus performed with 1024 near wake panels (around 17 rotations) in the flexible case and the obtained force distribution is depicted in Figure 1. The increased number of panels do not lead to any visible change in the force distribution in the case. As a result, the obtained C_T changes from 0.813521 with 600 panels to 0.813518 with 1024 panels, and the C_P varies from 0.600634 to 0.600631. Both Table 1 and Figure 4 are thus unaffected by the length of the near wake.

The result with 1024 panels are thus presented in the paper, and a mention to this verification has been added in the revised version:

This wake length was verified to be sufficient in this case to provide a converged force distribution on the blades by comparing to simulations with shorter near wake with 600 panels extending for 10 rotations, which led to the same results.

Comment 5 In figure 4: The results from OLAF show a small peak near the tip, which looks unusual. Please explain it and show that it is not dependent on the choice of parameters.

[1] https://github.com/IEAWindTask37/IEA-15-240-RWT/tree/master/OpenFAST/IEA-15-240-RWT-OLAF

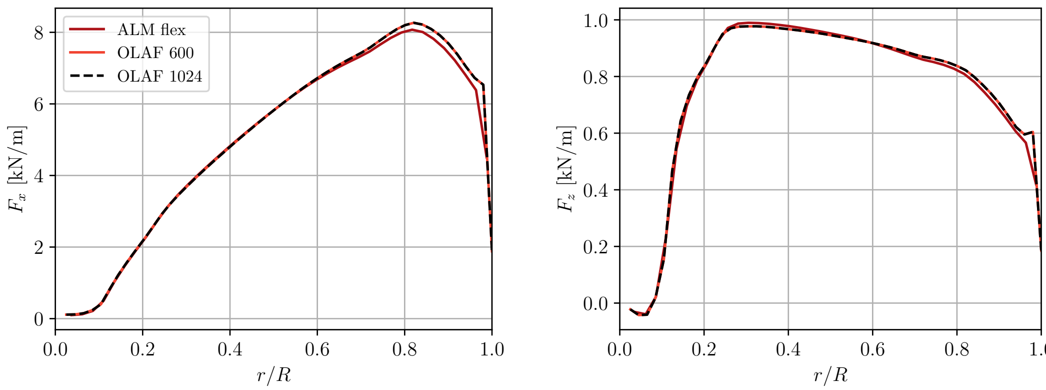

Figure 1: Steady state aerodynamic loads in the blade root frame for the flexible cases: ALM (dark red), and OLAF with 600 (light red) and 1024 near wake panels (dark dash).

Reply This peak arises from the regularization of the trailing vortex filaments using OLAf. It is similar to what is generally observed for the ALM with 3D mollification (see e.g. Meyer Forsting et al. (2019)). Due to the vortex filament regularization in the spanwise direction, the velocity induced by the trailing vortices decreases near the blade tip. This leads to a lower induced angle of attack and therefore to higher forces near the tip. The presented ALM does not show such a peak thanks to the use of a 2D mollification.

Since this peak is related to the regularization of the vortex filaments, it is affected by the parameters of the regularization. The parameters suggested in the reference IEA-15 MW model were used, as mentioned in the original manuscript : *"The vortex core is regularized using the Vatistas vortex model*[2] *with the optimized parameters option"*. The current implementation of the optimized parameters in OLAF consists in setting the vortex core radius r_c as twice the size of the spanwise spacing between the blade nodes Δs, hence here $r_c = 2\Delta s$, with $\Delta s \simeq R/50$. If one reduces the core radius to $r_c = 0.6\Delta s$, as suggested in the OLAF guidelines, the peak decreases but remains visible, as depicted in Figure 2. Similarly, if the node distribution changes and that the regularization scales with the spanwise discretization, then it will affect the peak at the tip.

We added a mention to the size of the regularization parameters in the set-up description: *The vortex core is regularized using the Vatistas vortex model with the optimized parameter option, which corresponds to using $r_c = 2\Delta s$ where Δs is the mean spanwise spacing between the aerodynamic nodes. Clearly, the regularization parameter can noticeably affect the force distribution, especially near the tip.*

The comment of the result has also been extended to discuss the effect of the regularization in more details:

The only noticeable difference between the two methods is the small increase of the forces near the blade tip, which is more pronounced using OLAF. The latter is due to the regularization of the trailing vortex filaments, which decreases the induced velocity near the tip. To a smaller extend, the ALM also depicts a slight increase of the lateral forces (i.e., F_z, in the blade root frame) at the tip due to the mollification (i.e., the smearing of the shed vortices (Caprace et al., 2019)). It is however less pronounced thanks to the use of the 2D mollification, without spanwise

[2] By the way, this model goes back to the regularization by Rosenhead (1935) of point vortices, where $1/r = r/r^2$ is replaced by $r/(r^2 + r_c^2)$ and should not be refered to Vatistas.

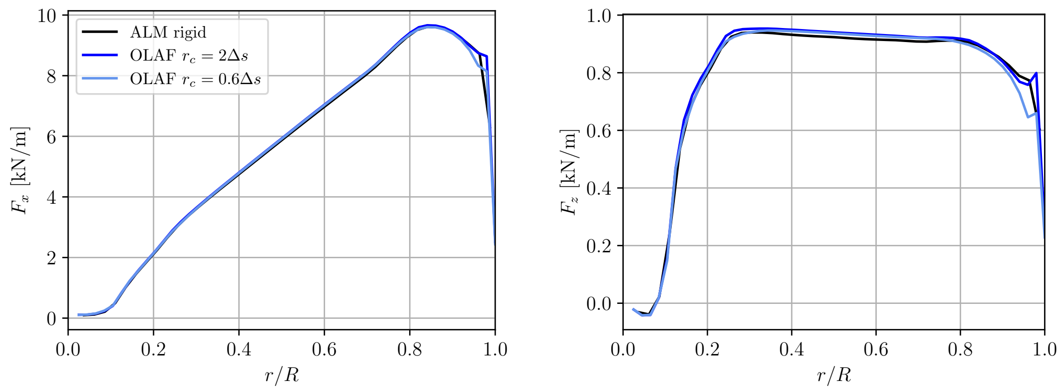

Figure 2: Steady state aerodynamic loads in the blade root frame for the IEA-15 MW with rigid blades: comparison between the ALM (black), and OLAF with two different regularization sizes.

smearing.

Comment 6 In line 202: Please define "lateral forces".

Reply A definition was added: *lateral forces (i.e., F_z, in the blade root frame).*

Comment 7 In line 205: Please cite (Caprace et al., 2019) when mentioning the error of the mollification of the ALM. That work clearly showed an error in the induced velocity for the choice of smearing used in the present work (2D Gaussian).

Reply The reference has been added. (By the way, this paper is from our research group)

Comment 8 It is relevant to cite (Mikkelsen, 2004) in the introduction and in the discussion of section 3.1 (lines 202 to 206). This work showed, in 2004, that an uncorrected 2D Gaussian had better results than an uncorrected 3D Gaussian. Also, the same work showed that the ALM with a 2D Gaussian regularization without tip correction predicted higher forces than methods (ALM and ADM) with Prandtl's (or Glauert's) tip correction. (Mikkelsen, R.F., 2004. Actuator disc methods applied to wind turbines, PhD Thesis, DTU, Chapter 8).

Reply Thank you for suggesting this reference. It is indeed relevant and has been added in Section 2.2 in which the ALM with 2D regularization is presented.

Comment 9 In lines 230 to 235: It is mentioned that the blade natural frequencies are calculated using the undeformed configuration. However, the flexible blades oscillate around the mean deformed configuration. For a non-linear solver such as BeamDyn, are the differences in the natural frequencies negligible?

Table 1: Natural frequencies (Hz) of the IEA-15 MW reference wind turbine obtained using BeamDyn for the blade rotating at 6.45 RPM.

	Undeformed	Deformed
1st Flapwise	0.518	0.516
1st Edgewise	0.736	0.734
2nd Flapwise	1.361	1.356
2nd Edgewise	2.547	2.538
3rd Flapwise	2.860	2.849
3rd Edgewise	4.625	4.607
1st Torsion	4.832	4.815

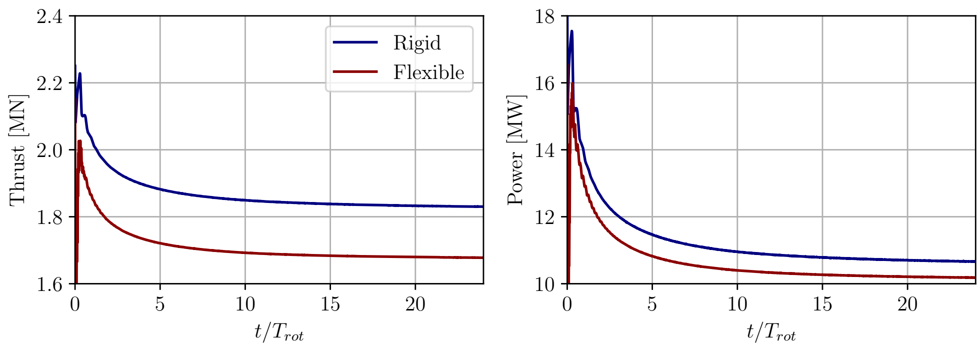

Figure 3: Evolution of the thrust and power with the number of rotation for the IEA-15 MW turbine with a uniform inflow velocity of 9 m/s.

Reply There is indeed a small effect of the deformation over the blade natural frequencies, as shown in Table 1. This Table compares the natural frequencies obtained using the undeformed blade position to those obtained by linearizing around the mean deformed configuration. The impact of the deformation over the natural frequencies is very limited, such that it can be considered negligible.

We added a mention to this investigation in the revised manuscript :

The blade natural frequencies are also depicted. These were obtained using the mass and stiffness matrices provided by BeamDyn in the rotating undeformed configuration, without accounting for the coupling with the aerodynamic loads. It should be noted that, for a non-linear beam solver, such as BeamDyn, the blade natural frequencies are slightly affected by the deformation. This difference was here verified to be negligible, such that the natural frequencies do not need to be updated using the blade deformed configuration.

Comment 10 In line 269: It is not clear that the value of 20 rotations for the discarded time is sufficient to reach a statistically stationary flow (it seems to be much lower than one flow through time). Please show that this choice does not affect the statistics.

Reply The convergence of the loads was tested in uniform flow according to the set-up presented in Section 3.1. The evolution of the power and thrust with the number of rotation is depicted in Figure 3. From rotation 20 to rotation 22, the thrust decreases by only 0.20% and the

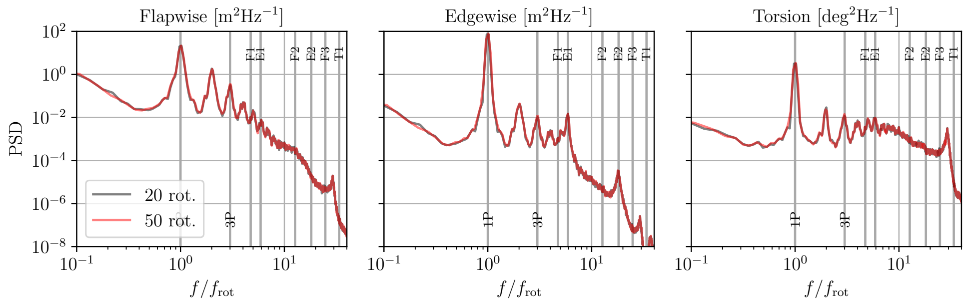

Figure 4: Power spectrum of the tip displacements for the IEA-15 MW turbine in ABL. Statistics are started after 20 or 50 rotations.

power decreases by 0.15%, which indicates that 20 rotations are sufficient to obtain statistically converged loads on the rotor. Twenty rotations is around 167 s, which is indeed smaller than one flow-through time (here, 0.58 flow-through time). For the loads, it is however not necessary to perform a full flow-through time to reach statistical convergence, since the far wake has a limited impact on the aerodynamics. The PSD of the displacements (Figure 6 of the original manuscript) was obtained by discarding the first 20. To verify the statistical convergence, it was re-computed by discarding the first 50 rotations. The differences are very small, as depicted in Figure 4.

This verification is mentioned in the revised manuscript :

The 20 first rotations are discarded as the wake induction is not yet converged. The power, thrust and power spectra of the loads were indeed verified to reach statistical convergence after 20 rotations.

Comment 11 In line 394: Analogously to the previous remark. Please show that this choice of "last 150 rotations" does not affect the statistics. How many flow through times were discarded?

Reply The 50 rotations have a duration of 417 s, corresponding to 1.45 flow-through time. This provides a sufficient buffer for the transient part of the wake to leave the computational domain. This is illustrated in Figure 5 which shows the velocity in the wake of the turbine at different normalized time $t^* = t\,U_{hub}/L_x$, where $L_x = 12D$ and $U_{hub} = 10$ m/s. One clearly observes that the transient part of the wake has reached the end of the domain for $t^* = 1.5$. Additionally, Figure 6 (corresponding to Figure 13 of the original manuscript) compares the velocity deficit and the turbulent kinetic energy profile obtained by collecting the flow statistics discarding the first 50 or the first 100 rotations. The statistics are quite similar, especially in the near wake. Some slight differences can be observed downstream, and result from the smaller averaging window. Clearly, these changes do not affect the discussion of the results in the original manuscript.

We mention this verification in the revised manuscript:

The wake statistics are first considered. The statistics are computed over the last 150 rotations, to ensure that the wake is developed up to the end of the computational domain before averaging. The discarded first 50 rotations corresponds to approximately 1.5 flow-through times, which was verified to be sufficient to reach a statistically converged flow. The averaging window of 150 rotations then corresponds to approximately 4.4 flow-through times.

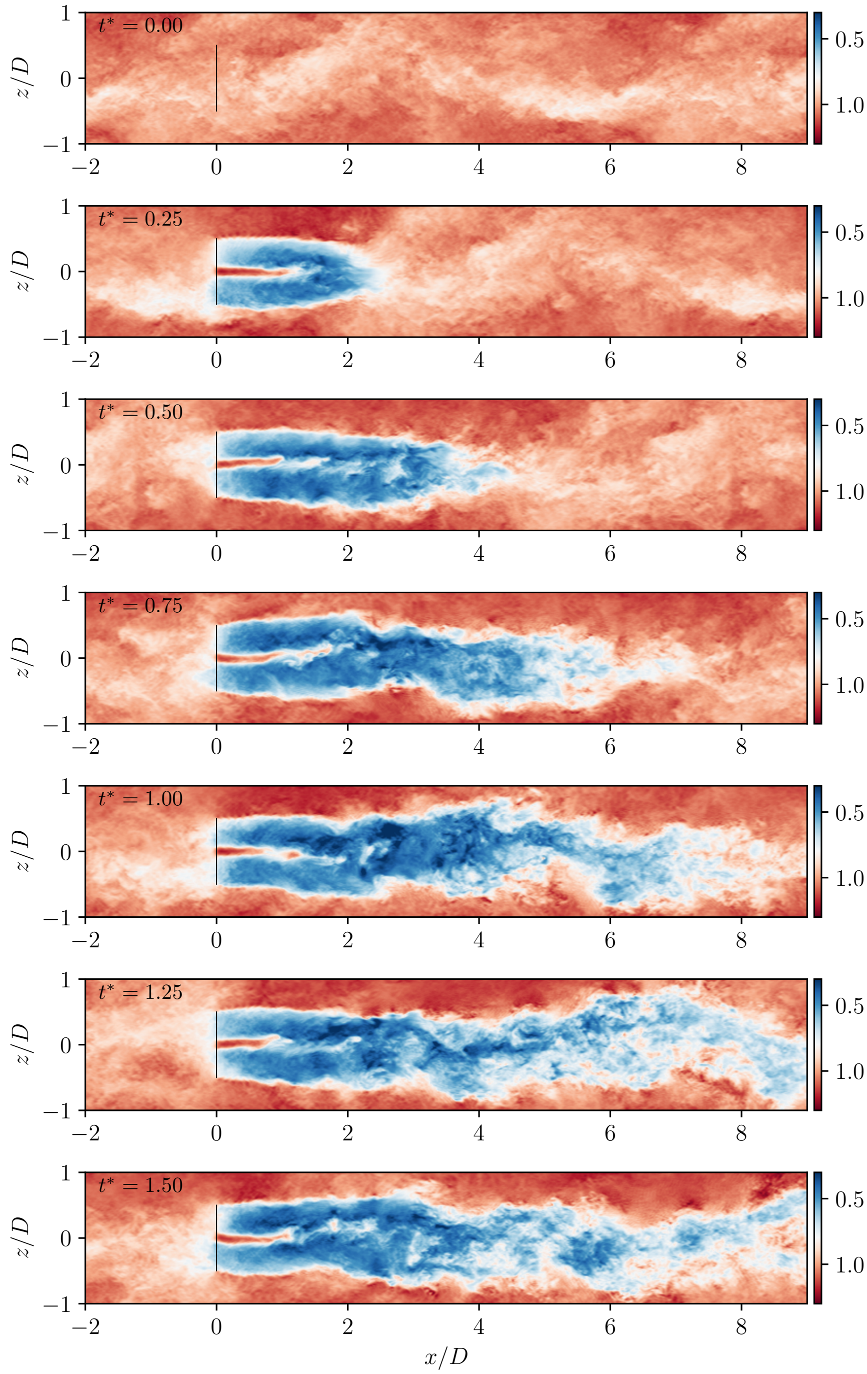

Figure 5: Instantaneous velocity in the horizontal plane crossing the rotor hub (bottom view).

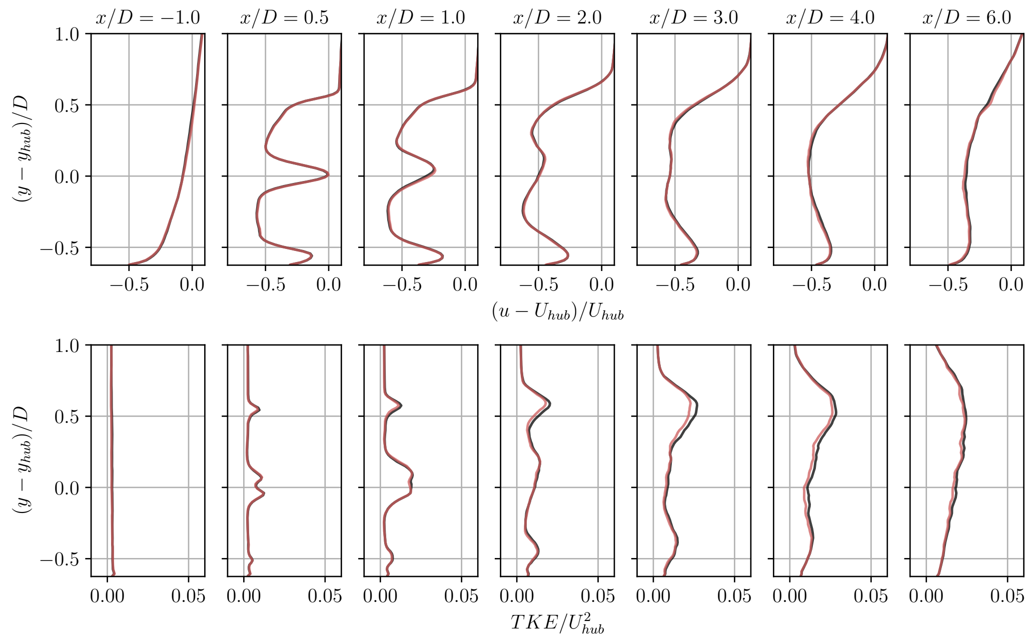

Figure 6: Profiles of mean velocity deficit (top) and turbulent kinetic energy (bottom) in the near wake of the turbine at various downstream locations. The flow statistics are obtained by discarding the 50 first rotations (black) or the 100 first rotations (red).

References

Caprace, D.-G., Chatelain, P., and Winckelmans, G.: Lifting line with various mollifications: theory and application to an elliptical wing, AIAA Journal, 57, 17–28, 2019.

Jha, P. K. and Schmitz, S.: Actuator curve embedding–an advanced actuator line model, Journal of Fluid Mechanics, 834, R2, 2018.

Meyer Forsting, A. R., Pirrung, G. R., and Ramos-García, N.: A vortex-based tip/smearing correction for the actuator line, Wind Energy Science, 4, 369–383, 2019.

Mikkelsen, R. F.: Actuator disk methods applied to wind turbines, 2004.

Investigation of blade flexibility effects over the loads and wake of a 15 MW wind turbine using a flexible actuator line method

Reply to reviewer 1

F. Trigaux, P. Chatelain, and G. Winckelmans

May 2024

We would like to thank the reviewer for the in-depth review and the insightful comments. All the comments have been addressed. The detailed reply to most of the comments is presented hereunder, as well as the suggested changes to the manuscript. Nevertheless, some small comments have been answered directly in the PDF file annotated by the reviewer, which is provided at the end of this document. The reviewer can also refer to the updated version of the manuscript, where all the changes are highlighted.

The authors thoroughly investigate the effect of blade flexibility on loads and wake behaviour using LES simulations with a flexible actuator line coupled to a structural solver. Their results and conclusions present a significant contribution in their field and they are presented with great quality. Overall it is very nice to read with maybe a few wording issues here and there.

There are few comments that the authors should address in the attached document before acceptance, mainly concerning the actuator line implementation, numerical sensitivity and analysis of the flowfield.

Reply Thank you for your appreciation. We are happy to read that the reviewer considers this work as a significant contribution to the field.

Comment 1 [l. 95 "Using the effective velocity at the control point"]: This is contradictory to the description in the following sentence. You are not using the velocity at the CP (single-point velocity interpolation) but are using a weighted average of the velocities around the CP., correct?

Reply This is correct, the "effective" velocity at the control point is taken as a weighted average of the local flow velocity. The sentences have been clarified:

The blades of the turbine are first discretized into a series of segments at the center of which a control point is placed, coinciding with the aerodynamic center of the corresponding airfoil profile. The components of the aerodynamic force acting on each cross-section are computed using the effective flow velocity associated to the control point and the lift and drag coefficients of that airfoil. This effective velocity is obtained in two steps. First, the velocity at the flow solver grid points is interpolated to the nodes of a 2D template centered on the control point. The template is depicted in Figure 1 and lies in the airfoil plane which is perpendicular to the actuator line, and is divided into cells of size h equal to the flow grid spacing. Then, the effective velocity is taken as a weighted average of the velocities on the template, using Gaussian weights.

Comment 2 [l. 96 "This effective velocity is obtained by interpolating the velocity at the flow solver grid points to the nodes of a 2D template centered on the control point and lying in the airfoil plane"]: That is a lot of interpolation. Did you evaluate the cost of these operations and the error this introduces in your velocity vector? The weighting probably helps smoothing the result but does not eliminate interpolation errors.

Reply This step indeed requires a significant number of interpolations. Each Gaussian template has 9×9 nodes on which the flow velocity must be interpolated. The cost of this operation is therefore non-negligible, especially since the interpolation requires a MPI communication between the processes of the flow solver that are close to the interpolation point. To optimize this process, we carefully grouped these communications to send a single buffer containing the velocities for all the interpolation points instead of doing a communication for each interpolation. We also defined sub-communicators for the turbine (see Appendix A). As a result, the cost of these interpolations is not excessive, and certainly not a bottleneck for our computations.

As to the error, a compact linear interpolation from the nearest flow solver grid points to each node of the template is used. The associated "error" remains small given that the flow grid and template grid are quite fine and of equal size (we used at least 64 grid points per turbine diameter). The important point is that the transfer of information is conservative, as the template used is Gaussian, and the sum of its weights is unity.

We added a mention to this in the revised manuscript: *This procedure requires many interpolations, yet its computational cost is limited by grouping the interpolated velocity in a single buffer and performing the MPI communication once. The interpolation is conservative, as the template used is Gaussian, and the sum of its weights is unity.*

Comment 3 [l. 98: "The effective velocity is taken as a weighted average, using Gaussian weights"]: An interesting approach, but did you evaluate the influence of this choice on your load response? By averaging in space your aerofoil response is being filtered. How much depends on the kernel/grid size you choose.

Reply We agree that evaluating the velocity as a weighted average introduces some smoothing of the fluctuations. Nevertheless, the use of "integral sampling" reduces the uncertainty about the location where the flow velocity must be sampled Churchfield et al. (2017) and we obtained a better agreement with reference mean load distributions using this approach than using a direct interpolation. This smoothing is further discussed in Section 3.2 and we now refer to this Section in Section 2.2 in which the ALM is presented:

It should be noted that the use of integral sampling leads to some smoothing of the high frequency velocity fluctuations. This effect is discussed in Section 3.2.

The discussion of the smoothing of the velocity fluctuations at the higher frequencies has been extended :

"The amplitude of the peak is however slightly smaller for the ALM. Indeed, the values of the PSD at all the higher frequencies (larger than 20P) obtained using the ALM are smaller than those predict using OpenFAST. This is mostly related to the use of integral velocity sampling in the ALM, which leads to some smoothing of the fluctuations as the velocity is obtained as a weighted average. On the contrary, OpenFAST interpolates the velocity fluctuations directly to the nodes of the aerodynamic solver (BEM or OLAF). However, the amplitude of these differences is limited and the value of the PSD at the affected frequencies is much smaller than at the lower frequencies, which are predominant".

It is also discussed when evaluating the effect of the flow resolution on the blade root moment (Section 5):

"For higher frequencies, the loads predicted using 128 pts/D are higher. This is due to the additional unsteadiness induced by the smaller turbulent scales that are resolved up to a higher frequency when at high resolution, and to the smaller mollification size that reduces the smoothing induced by the integral velocity sampling. "

Comment 4 [l. 110, about the use of 2D forces distribution and the necessity to use a smearing correction]: Having slender blades helps a lot, as the loading decreases slowly towards the tip. When inspecting Fig.4 it is possible to see the influence of not having a vortex core correction towards the very tip of the blade (the small discontinuity). The core correction also helps recovering sectional interdependency, neighbouring sections start interacting, smoothing the load distribution. A 2D approach is especially problematic at the end of the blade, as this gives rise to a force discontinuity in the spanwise direction, which gives rise to numeric oscillations. This should be checked.
Depending on the blade design, loading and grid resolution one might get away not having a vortex core correction, but it will introduce errors, the question is how large they are.

Reply Figure 4 (of the original manuscript) indeed presents a small increase of the forces in the very near tip region, which is a consequence of the forces smearing. More specifically, it is related to the small spanwise force distribution that occurs when the 2D force distribution is distributed to the nearest flow grid points. If one uses a mathematically perfect 2D force distribution, such as the mollified lifting line presented in Caprace et al. (2019), this discontinuity does not appear. However, we agree that even using a perfect 2D force distribution, some errors remain, as also shown in Caprace et al. (2019). Using a smearing correction would likely remove both the discontinuity and further correct the effect of the 2D mollification. However, using a 2D force distribution already provides much improved results compared to a 3D distribution.

In fact, we have verified the impact of the 2D mollification on the behaviour of the tip vortices, compared to the 3D mollification, as part of thesis work and before submitting this paper. We here report a part of this investigation. We consider the case of a simple rectangular wing of aspect ratio $AR = b/c = 7.5$, where b is the wing span and c the chord. The wing is modeled as an actuator line and has an angle of attack of 5^o. The flow grid resolution is $h/b = 1/128$. The results of this investigation is depicted in Figure 1. The use of 2D and 3D Gaussian mollification kernels are here compared.

Concerning the span loading, the ALM is here compared to the Prandtl Lifting Line (PLL) solution without any mollification. The agreement with the PLL is much better for the ALM with 2D mollification than with 3D mollification. However, some deviation still remains, especially in the near tip region. (see Caprace et al. (2019))

The near wake behind the wing is noticeably affected by the type of mollification. In the 2D case, the initial tip vortex in the wing plane has an elliptical shape. In the 3D case, the tip vortex is much more smeared/diffused and thus it consists in a Gaussian-type axisymmetric vortex. With the 2D mollification, the advection of the tip vortex in the near wake results in some numerical oscillations. Although these oscillations were not a problem in our simulations, the presence of sharp gradients in the vorticity field could be problematic for the numerical stability of some numerical methods. As expected, the tip vortex produced with 3D mollification is advected without numerical oscillations. Further in the wake ($x/b = 2$), the amplitude of the numerical oscillations when using the 2D mollification is reduced, and the tip vortex is essentially

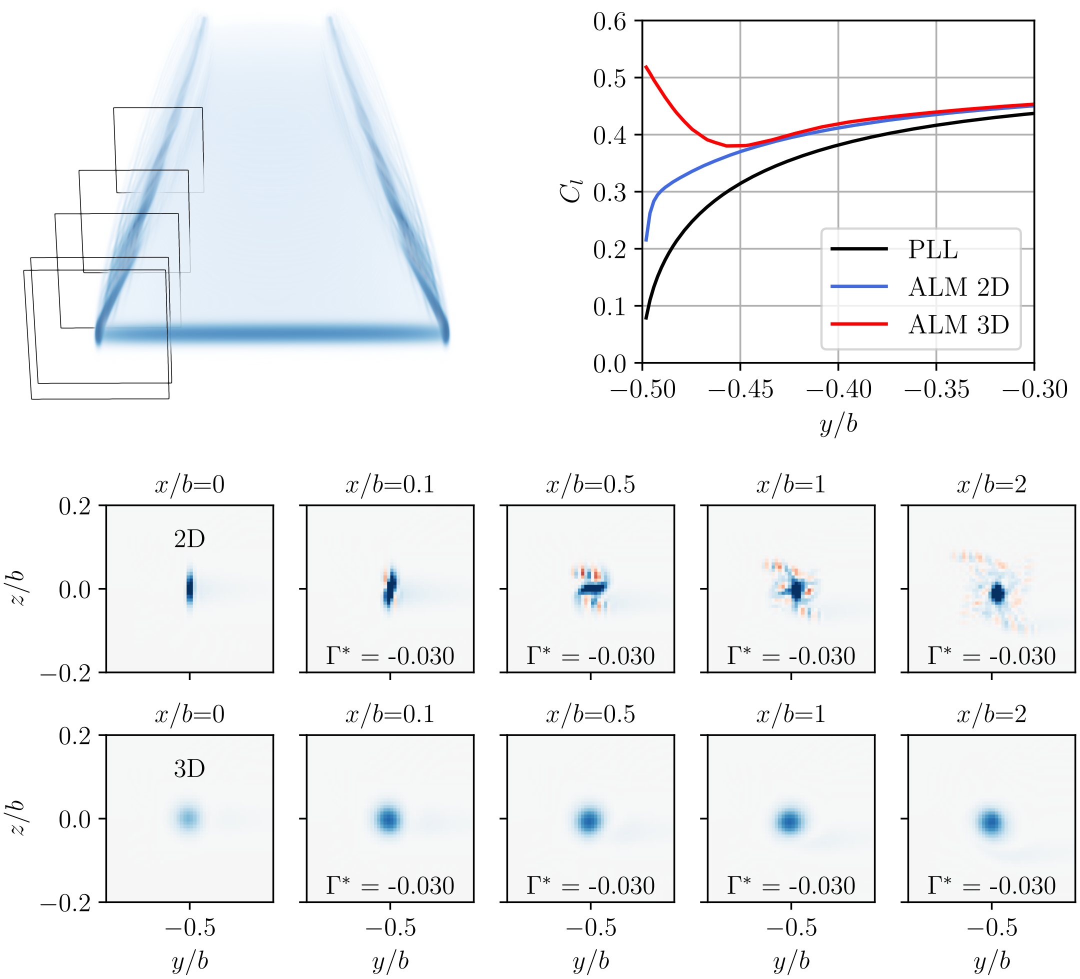

Figure 1: Investigation of the effect of the mollification for a rectangular translating wing of $AR = 7.5$ at an angle of attack of 5°, with a mollification $\sigma/c = 1/4$ and using a fine numerical resolution of $h/\sigma = 1/4$. Top left: 3D volume rendering of the vorticity magnitude in the wake of the 2D ALM, and location of the measured planes. Top right : Lift force distribution near the wing tip for the different mollification compared to the PLL. Bottom: planes of streamwise vorticity behind the left tip when using 2D (top) and 3D (bottom) mollifications.

axisymmetric, and with a smaller core radius than when using the 3D mollification. Additionally, the total circulation computed as the integral of the vorticity in the subdomain of Figure 1 is the same for both 2D and 3D mollifications. Hence, it is expected that the small scale numerical oscillations around the vortices in the near wake will not affect the flow dynamics away from these vortices and the loads on the blades.

Note that we also have a paper about these effect that is accepted for publication in the Journal of Fluid Mechanics and that will hopefully be published soon: F. Trigaux, T. Villeneuve, G. Dumas, G. Winckelmans, *Near tip correction functions for the actuator line method to improve the predicted lift and drag distributions*, Journal of Fluid Mechanics, 2024.

We added a mention to this investigation in the paper (section 2.2 related to the use of the 2D mollification for the ALM): *Note that the shape of the tip vortices is affected by the type of mollification, and that the use of a 2D mollification result in sharp force gradient that can lead to numerical oscillations in some numerical methods. These were here verified to be of small amplitude, and do not affect the flow dynamics away from those vortices and the loads on the blades.*

Comment 5 [l. 176, Relative to the resolution of 64 pts/D and the use of integral sampling]: This means that the kernel size is 7.5m, correct? That in connection with the weighted velocity sampling, means that velocities are quite heavily averaged in space (consider kernel size over free-stream for instance 7.5/9 = 0.83 seconds). In uniform inflow this does of course not matter, but in turbulent inflow it could. Was this checked?

Reply The kernel size is indeed 7.5 m and it leads to a smoothing of the high frequency load fluctuations. This is discussed in more details at the end of Section 3.2 which compares the blade tip displacements obtained in turbulent flow to those obtained using OpenFAST (see Comment 3).

As a side note, one should also consider that most of the unsteady loads arise from the blade rotation in the turbulent wind with spatially coherent structures. As a result, for most of the blade, the effect of the averaging should be considered using the rotation speed Ωr rather than the free stream velocity. Since the tip-speed ratio is here $TSR = 9$, this leads to a much higher cut-off frequency.

Comment 6 [l. 200, Relative to the OLAF results]: Why is there such a pronounced kink in the OLAF simulations towards the tip? Is that related to the node distribution?

Reply This peak arises from the regularization of the trailing vortex filaments using OLAf. It is similar to what is generally observed for the ALM with 3D mollification (see e.g. Meyer Forsting et al. (2019)). Due to the vortex filament regularization in the spanwise direction, the velocity induced by the trailing vortices decreases near the blade tip. This leads to a lower induced angle of attack and therefore to higher forces near the tip. The presented ALM does not show such a peak thanks to the use of a 2D mollification.

Since this peak is related to the regularization of the vortex filaments, it is affected by the parameters of the regularization. The parameters suggested in the reference IEA-15 MW model were used, as mentioned in the original manuscript : *"The vortex core is regularized using the Vatistas vortex model*[1] *with the optimized parameters option"*. The current implementation of

[1]By the way, this model goes back to the regularization by Rosenhead (1935) of point vortices, where $1/r = r/r^2$ is replaced by $r/(r^2 + r_c^2)$ and should not be refered to Vatistas.

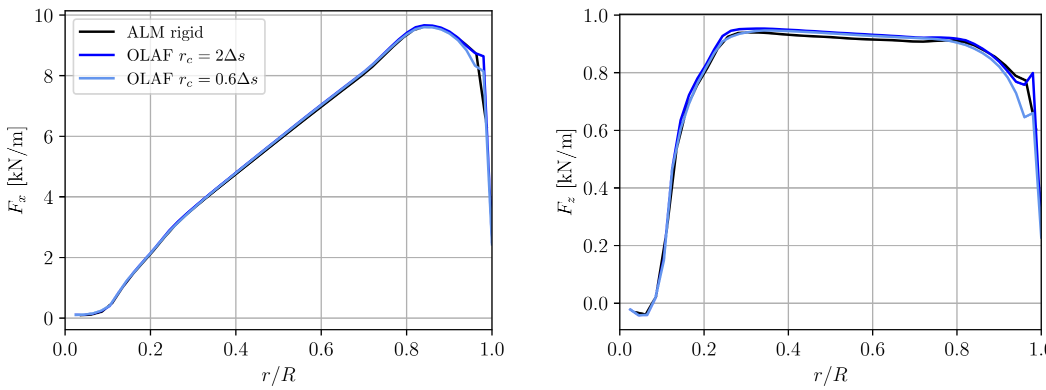

Figure 2: Steady state aerodynamic loads in the blade root frame for the IEA-15 MW with rigid blades: comparison between the ALM (black), and OLAF with two different regularization sizes.

the optimized parameters in OLAF consists in setting the vortex core radius r_c as twice the size of the spanwise spacing between the blade nodes Δs, hence here $r_c = 2\Delta s$, with $\Delta s \simeq R/50$. If one reduces the core radius to $r_c = 0.6\Delta s$, as suggested in the OLAF guidelines, the peak decreases but remains visible, as depicted in Figure 2. Similarly, if the node distribution changes and that the regularization scales with the spanwise discretization, then it will affect the peak at the tip.

We added a mention to the size of the regularization parameters in the set-up description: *The vortex core is regularized using the Vatistas vortex model with the optimized parameter option, which corresponds to using $r_c = 2\Delta s$ where Δs is the mean spanwise spacing between the aerodynamic nodes. Clearly, the regularization parameter can noticeably affect the force distribution, especially near the tip.*

The comment of the result has also been extended to discuss the effect of the regularization in more details:

The only noticeable difference between the two methods is the small increase of the forces near the blade tip, which is more pronounced using OLAF. The latter is due to the regularization of the trailing vortex filaments, which decreases the induced velocity near the tip. To a smaller extend, the ALM also depicts a slight increase of the lateral forces (i.e., F_z, in the blade root frame) at the tip due to the mollification (i.e., the smearing of the shed vortices (Caprace et al., 2019)). It is however less pronounced thanks to the use of the 2D mollification, without spanwise smearing.

Comment 7 [Page 11: "Some additional differences in the lower frequency part of the spectrum are related to changes in the turbulent fluctuations during their convection from the inflow to the turbine location]: Was a simulation without turbine performed as well to check this?

Reply A simulation without a turbine was performed to assess the evolution of the synthetic turbulence when added to a LES domain in the numerical set-up presented in Section 3.2. Figure 3 shows that the TI decreases along the domain streamwise coordinate. This is expected from the fact that in the present case the Mann turbulence is added to a uniform inflow, hence there is no production of TKE during the convection: the TKE can only decrease. We here

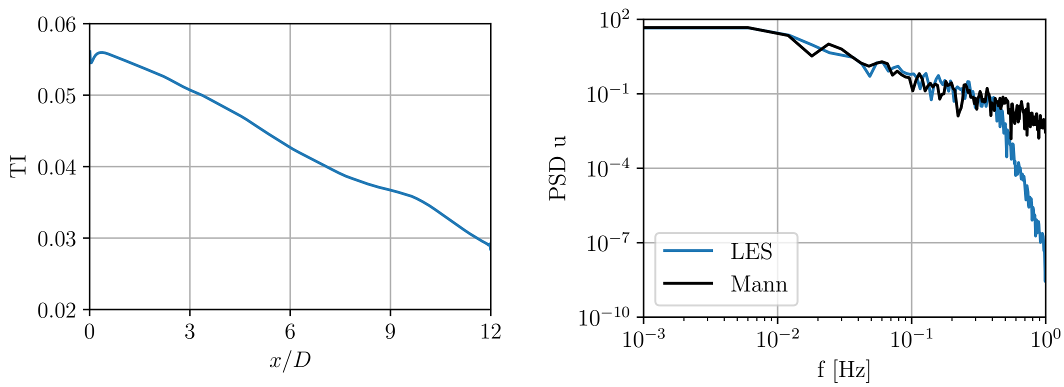

Figure 3: Left : Evolution of the turbulence intensity (TI) along the streamwise direction of the LES domain. Right : Power spectral density (PSD) of the streamwise velocity in the LES domain at the turbine location (LES) compared to that of the turbulent fluctuations generated using the Mann algorithm (Mann).

stress that our flow solver conserves the kinetic energy (Duponcheel, 2009), so that the decrease of the TI is not linked to spurious numerical dissipation. It is solely due to the dissipation by the subgrid-scale model and air viscosity. Figure 3 also shows the PSD of the streamwise velocity measured either in the LES domain at the turbine location or directly in the turbulence field generated using the Mann algorithm. One clearly observes the decrease of the higher frequencies in the LES, as well as some changes in the lower frequencies. These changes justify the observed variations between the ALM and OpenFAST.

The following sentence has been kept: *"Some additional differences in the lower frequency part of the spectrum are related to changes in the turbulent field during its convection from the inflow to the turbine location"*. Yet, the reference to Mann et al. (2018) is removed as it mostly concerns the effect of the induction on the turbulence, which is not the primary factor here.

Comment 8 [l. 249: About the location of the wind turbine at a distance 2D from the inflow]: This is extremely close to the inflow, the influence of this choice needs to be documented

Reply To document this effect, the simulation with flexible blades was again performed with an increased distance from the inflow: $4D$ instead of $2D$. There is indeed a small impact on the tangential load distribution, as depicted in Figure 4. The thrust coefficient decreases from 0.692 at a distance $2D$ to 0.683 (-1.3%) at a distance $4D$. The power coefficient evolves from 0.446 to 0.432 (-3.1%). The power spectrum of the loads is not noticeably affected by the change of the distance to the inflow, as depicted in Figure 5. Given the small changes in thrust and load distribution, the wake is virtually unaffected. Additionally, it should be noted that the three considered cases (rigid undeformed, rigid deformed and flexible) use the same numerical set-up, such that the effect of the distance to the inflow is the same for each simulation.

We have added a mention to this investigation in the revised manuscript: *The location of the turbine hub is* $(2D, y_{hub}, 2D)$*, where* $y_{hub} = 150$ *m. Although the distance between the turbine and the inflow is small, it has been verified to have a very small effect on the loads (approximately 1% difference on thrust and 3% difference on power when the distance to the inflow is doubled). Moreover, the same distance to the inflow is used for each considered case,*

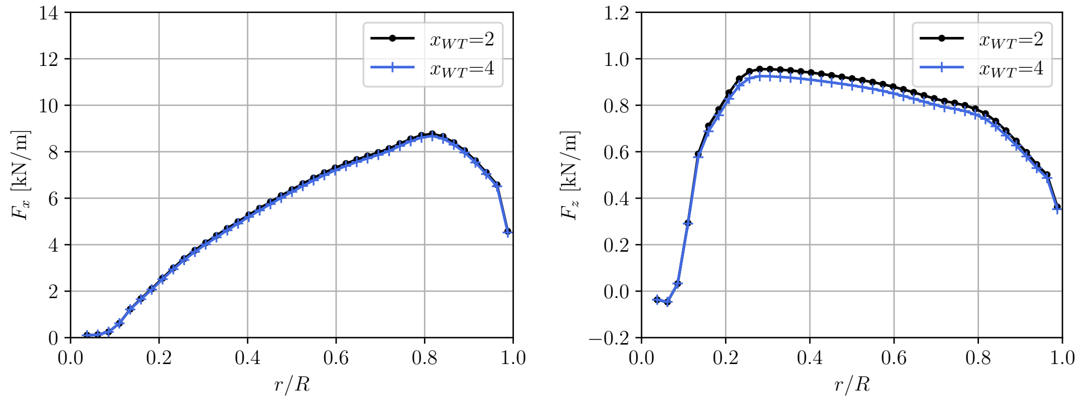

Figure 4: Influence of the distance of the wind turbine to the inflow on the mean normal and tangential force distribution.

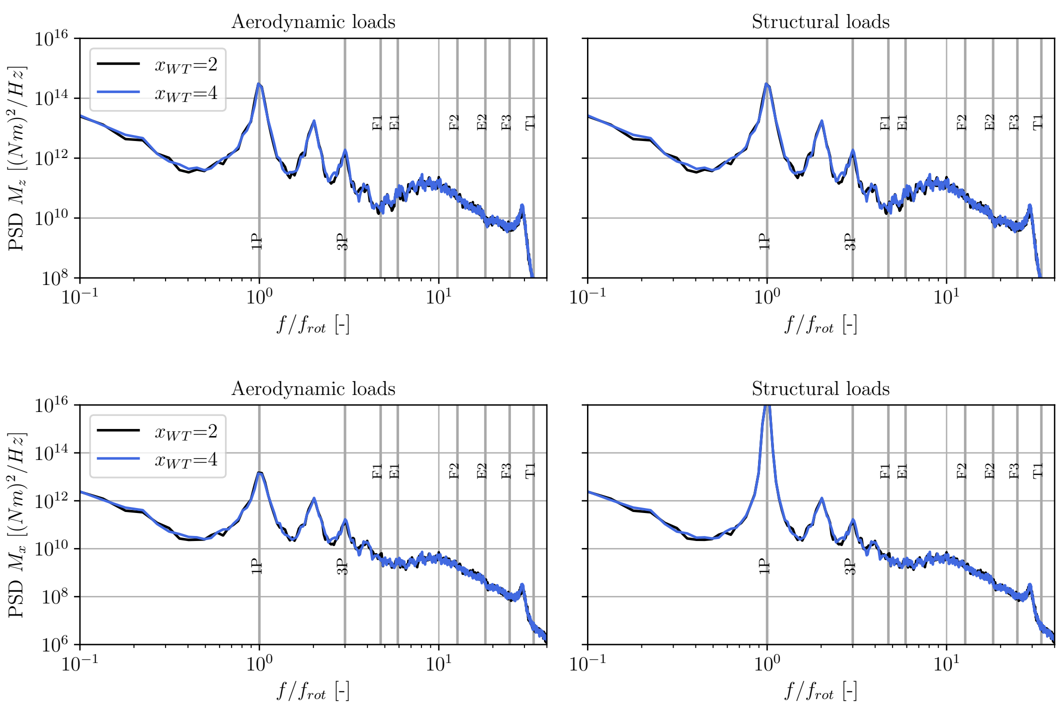

Figure 5: Influence of the distance of the wind turbine to the inflow on the PSD of the root bending moment in the flapwise (top) and edgewise (bottom) directions.

such that the comparison is not affected.

Comment 9 [l. 309: In reference to equation (1)] : So the AoA is computed without considering the curvature of the blade? The torsion is also in the blade root reference frame?

$$\alpha = \arctan\left(\frac{(v_x - v_{\text{struct},x})}{(v_{\text{struct},z} - v_z)}\right) + \phi_{struct,y} + \beta, \tag{1}$$

Reply Our code does account for the blade curvature: the flow velocity sampled at the control point is expressed in the local airfoil frame according to the orientation provided by the structural solver. The computed angle of attack hence intrinsically accounts for both the blade curvature and the torsion. Equation (1) here does not account for the the blade curvature and is used for the comparison if Figure 8 of the manuscript. If the effect of the blade curvature is assumed to be negligible for the computation of the angle of attack, then the torsion angle $\phi_{struct,y}$ can be viewed as an additional twist angle, and we indeed recover Equation (1). We also confirm that $\phi_{struct,y}$, as well as v and v_{struct} are then taken in the blade root frame.

The paragraph was reworked to clarify :

In fact, the angle of attack α of a section of the blade can be approximated using the flow and structural velocities expressed in the blade root frame by neglecting the effect of the blade curvature on the angle of attack,

$$\alpha \simeq \arctan\left(\frac{(v_x - v_{\text{struct},x})}{(v_{\text{struct},z} - v_z)}\right) + \phi_{struct,y} + \beta,$$

where v_x, v_z are the local flow velocities in the x (streamwise) and z (azimuthal) directions, $v_{\text{struct},x}$, $v_{\text{struct},z}$ are the local structural velocities in these directions, $\phi_{\text{struct},y}$ is the local torsion angle and β is the local twist angle. All these variables are here expressed in the blade root frame.

Comment 10 [l. 388 : "The wake can be affected in two ways"]: Three ways really, it can change the magnitude of the wake deficit, as it will change the global and local C_T. If the C_T changes it cannot be expected that the wake will not change as well.

We initially included the effect of the change in thrust coefficient into the "variation of the loads" that leads to a change of the velocity deficit. We however reworked this paragraph to separate the effect of the thrust coefficient and of the load distribution.

The new paragraph reads as follows:

[...] The wake can be affected in three ways. Firstly, the changes in thrust coefficient C_T affect the total velocity deficit behind the turbine. Secondly, the variation of the load distribution along the blade span described in Section 4.2 changes the shape of the velocity deficit. If the loads decrease more smoothly near the tip, the strength of the tip vortices also decreases. Finally, the displacements of the blade described in Section 4.1 affect the location of the emission of the tip vortices. Specifically, the tip vortices are generated further downstream due to the flapwise bending, and the flexibility affects the distance between individual tip vortices, potentially modifying their interaction. [...]

Comment 11 [l. 424, about the wake comparison]: Whilst the snapshots are nice to look at, I would like to see spectra of the turbulence at different downstream positions or other high-order statistics compared. Snapshots are qualitative. Spectra could help discover potential differences.

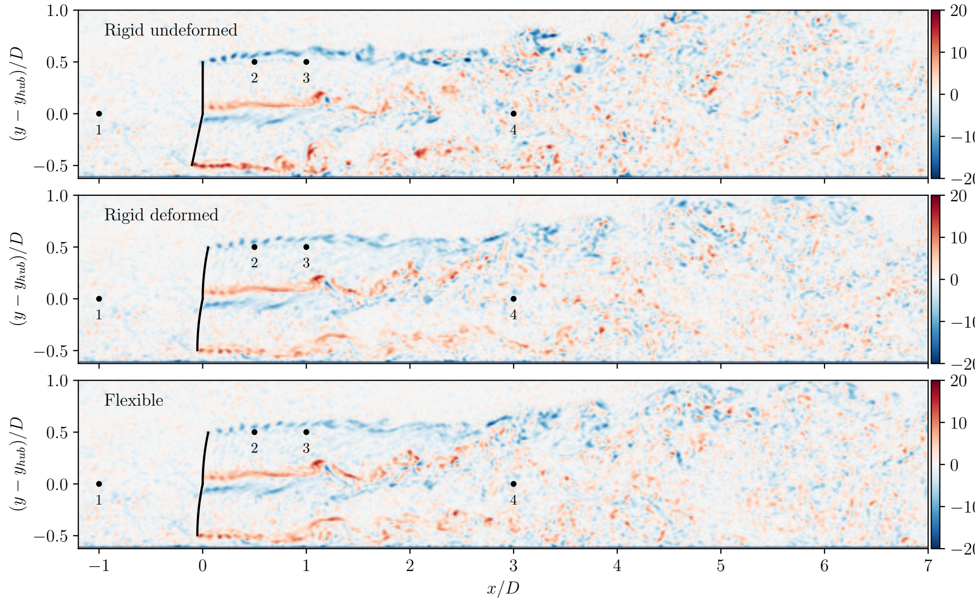

Figure 6: Snapshot of an instantaneous out-of-plane vorticity field ($\omega_z D/U_{hub}$) in the wake of the turbine for the rigid (top), deformed (middle) and flexible (bottom) cases. The inflow is identical for each case. The location of the probes used for the velocity spectra are also shown.

Your point is well taken, we have measured for spectra at location reported in Figure 6. Two paragraphs discussing these turbulence spectra and the wake recovery rate have been added to the revised manuscript. The paragraphs read as follows:

The streamwise velocity is measured at various locations in the wake for each case to compare the flow statistics. Four locations are selected, as depicted in Figure 6. The power spectral density of the streamwise velocity (obtained using the Welch algorithm) is then depicted for each case in Figure 6. The first location is $1D$ *upstream of the hub in the induction zone (Probe 1), and the three PSDs are virtually identical, which confirms that the differences in the downstream flow can be fully attributed to the changes in the turbine aerodynamics. The flow velocity is also sampled behind the blade tip at two positions. In the very near wake (*$0.5D$ *behind the rotor, Probe 2), the blade passing frequency is clearly noticeable for the deformed and flexible cases, whereas it is not visible in the rigid undeformed case. This can be related to the fact that the tip vortices are well separated at this location in the deformed and flexible cases, while they already merged into a vortex sheet in the rigid undeformed case. Additional differences can be observed further in the wake (*$1D$ *behind the rotor, Probe 3), where the rigid undeformed case presents a much higher PSD at the frequencies lower than 1P. This increase results for the destabilization of the vortex sheet, which results in lower frequency velocity variations. On the contrary, the rigid deformed and flexible cases do not exhibit such an increase, indicating that the wake remains stable at this location. Finally, the velocity is measured further downstream,* $3D$ *behind the hub (Probe 4), where the influence of the hub vortices is minimal. At this location, the three PSDs are similar. For each location, the differences between the rigid deformed and the flexible case are small, confirming the limited impact of the unsteady variations on the wake.*

The wake recovery rate is measured for each case by computing the power available in the flow P_w *on the rotor swept area* A_{rot}*. The latter is obtained as a function of the streamwise*

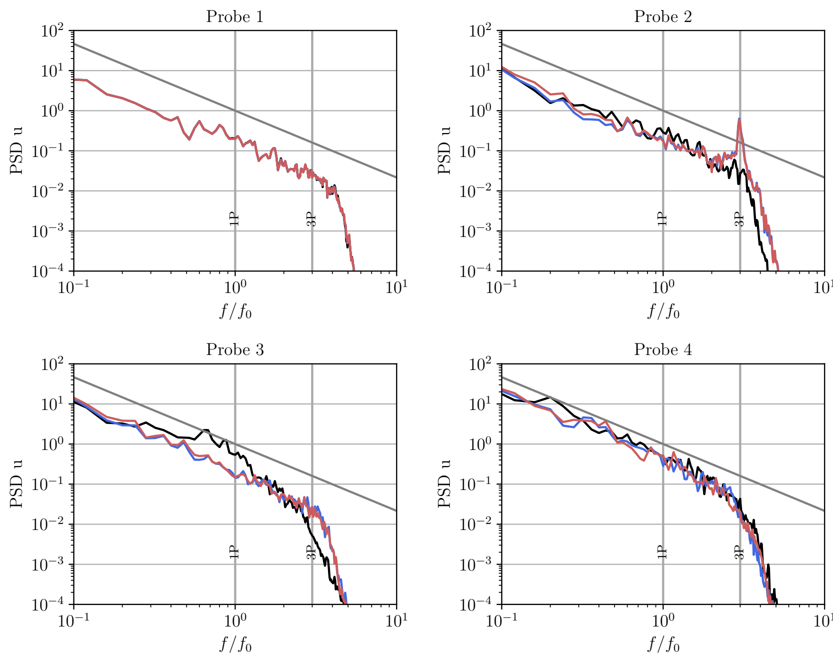

Figure 7: PSD of the streamwise velocity at various locations (as depicted in Figure 6).

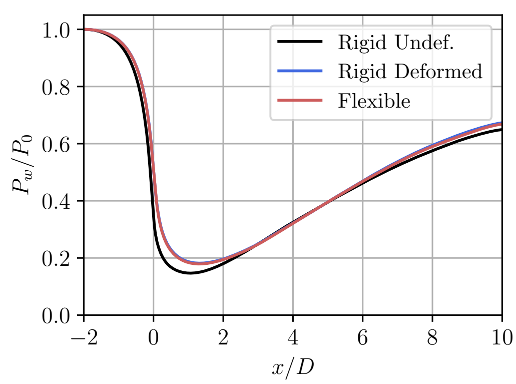

Figure 8: Available power in the wake (normalized by the power at the inflow), computed over the rotor swept are at various streamwise location.

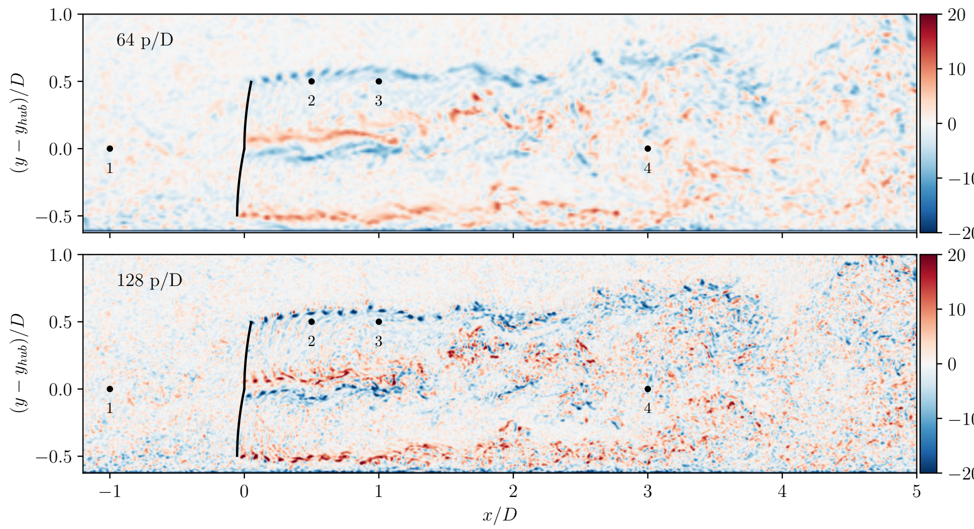

Figure 9: Snapshot of an instantaneous out-of-plane vorticity field ($\omega_z D/U_{hub}$) in the wake of the turbine for the 64 pts/D resolution (top) and the 128 pts/D resolution (bottom) cases. The inflow is identical for each case.

coordinate x as

$$P_w(x) = \frac{1}{2}\rho \iint_{A_{rot}} \bar{u}^3(x,y,z)\,dy\,dz. \tag{2}$$

The variation of the power (normalized by the power P_0 at the inflow) is depicted in Figure 8. The available power in the wake of the rigid undeformed case is lower in the near wake due to the higher thrust coefficient. It also presents a faster recovery rate since it reaches the same level as the two other cases for $2 < x/D < 6$. However, in the far wake, it is also slightly lower than in the rigid deformed flexible and cases. These two cases again present almost identical statistics.

Comment 12 [l. 460 : About the wake comparison at resolution 128 and 64 pts/D]: Spectra should be compared additionally or exclusively.

A discussion of the velocity spectra at various locations has been added to the paper:

The PSD of the streamwise velocity at various locations in the domain is also compared for both resolutions. The locations where the flow velocity is sampled is depicted in Figure 9 and the obtained spectra are depicted in Figure 10. The first spectra are obtained using the streamwise velocity measured $1D$ upstream of the hub (Probe 1). At this location, the PSD obtained for the simulation with 64 pts/D decreases much faster at higher frequencies, as expected from the smaller LES cut-off frequency. There are also some slight differences below the cut-off frequency due to the interpolation at the inflow from the ABL with 128 pts/D resolution to the LES with 64 pts/D resolution, and the variation occuring during the convection of the turbulence between the inflow and the sampling location. In the near wake, the PSD of the velocity measured $0.5D$ behind the blade tip (Probe 2) is very similar between the two resolutions (except at the highest frequencies). When measuring $1D$ downstream of the blade tip (Probe 3), the peak of the PSD obtained for the simulation with 128 pts/D is more pronounced near the 3P frequency, due to the more distinct tip vortices, whereas the tip vortices have merged into a vortex sheet in the

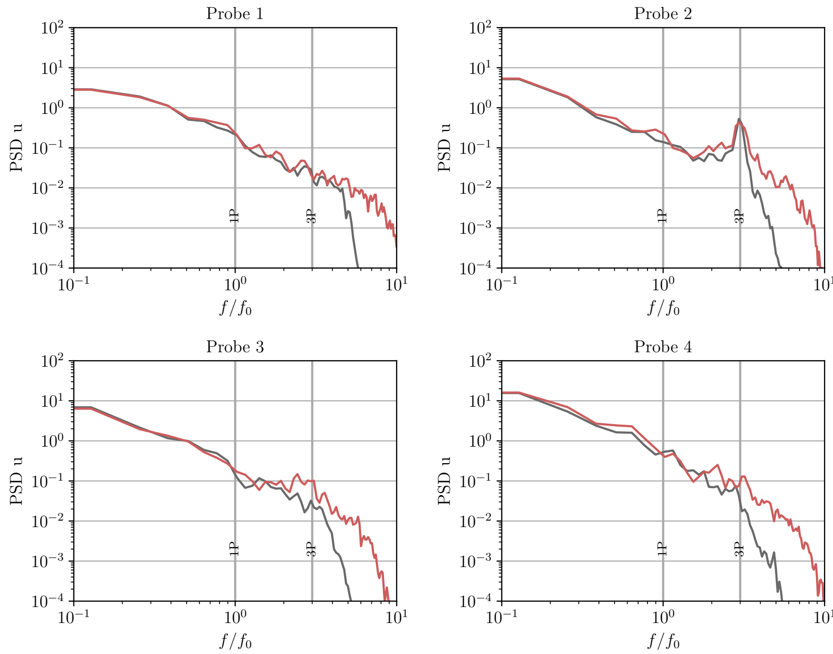

Figure 10: Comparison between the PSDs of the streamwise velocity at various locations (as depicted in Figure 9), obtained at a resoltion of 64 p/D and 128 p/D.

simulation with 64 pts/D. Further in the wake, 3*D behind the hub (Probe 4), the spectrum are in good agreement at the lower frequencies, and only show deviations at the higher frequencies.*

References

Caprace, D.-G., Chatelain, P., and Winckelmans, G.: Lifting line with various mollifications: theory and application to an elliptical wing, AIAA Journal, 57, 17–28, 2019.

Churchfield, M. J., Schreck, S. J., Martinez, L. A., Meneveau, C., and Spalart, P. R.: An advanced actuator line method for wind energy applications and beyond, 35th Wind Energy Symposium, p. 1998, 2017.

Duponcheel, M.: Direct and large-eddy simulation of turbulent wall-bounded flows : further development of a parallel solver, improvement of multiscale subgrid models and investigation of vortex pairs in ground effect, 2009.

Mann, J., Peña, A., Troldborg, N., and Andersen, S. J.: How does turbulence change approaching a rotor?, Wind Energy Science, 3, 293–300, 2018.

Meyer Forsting, A. R., Pirrung, G. R., and Ramos-García, N.: A vortex-based tip/smearing correction for the actuator line, Wind Energy Science, 4, 369–383, 2019.

https://doi.org/10.5194/wes-2024-19
Preprint. Discussion started: 19 February 2024

eawe european academy of wind energy
Open Access WIND ENERGY SCIENCE DISCUSSIONS

Investigation of blade flexibility effects over the loads and wake of a 15 MW wind turbine using a flexible actuator line method

Francois Trigaux[1], Philippe Chatelain[1], and Grégoire Winckelmans[1]

[1]Institute of Mechanics, Materials and Civil Engineering (iMMC), Université catholique de Louvain (UCLouvain), 1348 Louvain-la-Neuve, Belgium

Correspondence: Francois Trigaux (francois.trigaux@uclouvain.be)

Abstract.

This paper investigates the impact of the blades flexibility on the aerodynamics and wake of large offshore turbines using a flexible actuator line method (ALM) coupled to the structural solver BeamDyn in Large Eddy Simulations. The study considers the IEA 15-MW reference wind turbine in close-to-rated operating conditions. The flexible ALM is first compared to OpenFAST simulations and is shown to consistently predict the rotor aerodynamics and the blades structural dynamics. However, the effect of the blade flexibility on the loads is more pronounced when predicted using the ALM than using the blade element momentum theory. The wind turbine is then simulated in a neutral turbulent atmospheric boundary layer with flexible and rigid blades. The significant flapwise and torsional mean displacements lead to an overall decrease of 14% in thrust and 10% in power compared to a rotor with no deformation. These changes influence the wake through reduced time-averaged velocity deficit and turbulent kinetic energy. The unsteady loads induced by the rotation in the sheared wind and the turbulent velocity fluctuations are also substantially affected by the flexibility and exhibit a noticeably different spectrum. However, the influence of these load variations is limited over the wake, and the assumption of rigid blades in their deformed geometry is shown to be sufficient to capture the wake dynamics. The influence of the resolution of the flow solver is also evaluated, and the results are shown to remain consistent between different spatial resolutions. Overall, the structural deformations have a substantial impact on the turbine performance, loads and wake, which emphasizes the importance of considering the flexibility of the blades in simulations of large offshore wind turbines.

1 Introduction

Over the past years, offshore wind energy has grown massively thanks to a drastic decrease of its levelized cost of energy. This significant reduction is primarily attributed to the increase of the rotor size that tends to drive down both capital and operational expenditures. In fact, larger modern turbines typically exhibit a lower turbine cost per MW compared to their smaller counterparts. At the level of the wind farm, the decreased number of turbines also allows to reduce the cables requirements (Fingersh et al., 2006). The cost of maintenance per MW was also reported to be by a few percent lower per additional MW of rated power (Sørensen and Larsen, 2021). Furthermore, larger turbines typically have higher hub heights, which results in a more important mean flow velocity across the rotor and hence to an increased power extraction per unit area (Sørensen and Larsen,

https://doi.org/10.5194/wes-2024-19
Preprint. Discussion started: 19 February 2024

2023). As a result, turbines with a rated power of 10-12 MW are now commonly used in offshore conditions, and the industry is rapidly developing 15-18 MW prototypes with blades much longer than 100 m.

However, as the rotor diameter increases, fundamental changes of design are necessary to constrain the total mass of the blades to reduce the centrifugal and gravitational loads acting upon them (Sieros et al., 2012). Therefore, recent blades are slender and made of lightweight composite materials, increasing their flexibility and potentially causing significant aeroelastic effects. The structural deformation of the blades modifies their aerodynamics by adding bending and twist, which can lead to substantial changes of the mean loads acting on the turbine. Additionally, the wind shear and turbulence create unsteady aeroelastic effects that impact the turbine lifetime. These variations can ultimately affect the flow past the turbine, modifying the wake evolution and recovery. A deeper understanding of the loads and wake of these large turbines is required to design reliable products and predict their interaction in a wind farm, which will allow to further reduce the cost of the offshore wind energy.

The structural aspect is often neglected in simulations that use the actuator line or disk methods to represent the flow past a turbine. Whereas this approach was mostly valid for smaller turbines, the flow past large rotors is now noticeably affected by the changes of the aerodynamics. To evaluate these effect, some studies have considered the coupling of a flow solver to a structural solver using actuator methods as interface. Storey et al. (2013) coupled OpenFAST to an actuator disk method to perform simulations of one or two turbines and to compare their results to measurements. Vitsas and Meyers (2016) used a modal structural model coupled to an actuator sector method to study two wind farm configurations. More recently, OpenFAST was also coupled to Nalu-Wind and PALM (Sprague et al., 2020; Krüger et al., 2022) to study the NREL-5 MW reference wind turbine. Hodgson et al. (2021) also performed validation of flexible actuator methods against high fidelity blade-resolved simulations, highlighting the ability of the ALM to accurately capture aeroelastic effect on rotors up to 5 MW (see also Sørensen et al. (2015); Hodgson et al. (2022)). An elastic ALM based on the coupling between an ALM and an Euler beam model discretized using finite differences was also developed by Meng et al. (2018, 2020), and used for a pair of NREL-5 MW turbines and a wind farm. Spyropoulos et al. (2021) also developed a fluid-structure interaction framework based on the ALM in a flow solver for the compressible URANS equations. That framework uses a multi-body formulation with Timoshenko beam elements to solve the structural dynamics. It was compared in uniform flow against the Blade Element Momentum (BEM) theory and a lifting line, and was show to accurately predict the blade deflections and the loads, also in yawed conditions. Della Posta et al. (2022, 2023) also considered a two-way coupling between a structural solver and an ALM, including the tower, for unsteady aerodynamics of the NREL-5 MW rotor. However, most of the aforementioned studies consider medium-scale rotors with simpler structural parameters than the new generation turbines. Consequently, the effect of the non-linearities induced by the large displacements are not considered. Additionally, the impact of the flexibility is rarely assessed by comparing the results to those obtained for rigid blades. Finally, most of the studies focus on the blade and rotor loads, but do not assess the effect of the flexibility on the wake in depth.

This study investigates the effects of the deformation of the rotor on a very large reference wind turbine in realistic operating conditions. The open-source IEA 15-MW (Gaertner et al., 2020) turbine model is selected for its large rated power that is representative of modern large-scale offshore turbines and for its comprehensive documentation. Large Eddy Simulations of the

https://doi.org/10.5194/wes-2024-19
Preprint. Discussion started: 19 February 2024

atmospheric boundary layer and of the wake of the turbine are carried using a flexible ALM coupled to the nonlinear structural solver *BeamDyn* from OpenFAST. Comparison between fully coupled aeroelastic simulations and simulations assuming rigid blades aims at providing a deeper understanding into the variation of the loads induced by the flexibility. Then, the effect of the blade displacement and of the loads variation is assessed over the wake. The contribution of this study is therefore to provide further insights into the effect of the mean and unsteady deformations over the loads of the 15 MW turbine and to evaluate their impact on the wake.

This paper is structured as follows. The methodology is presented in Section 2, which describes the flow solver, the embedded flexible ALM and the coupling with the structural solver. Then, Section 3 presents a comparison between results obtained with the flexible ALM to those obtained using OpenFAST simulations. Performed in both uniform and turbulent flows, this comparison also aims at verifying the results obtained with the flexible ALM and at assessing the relevance of the various aerodynamic models for the simulation of large flexible wind turbines. The case of a wind turbine in realistic atmospheric conditions is then investigated in Section 4, where comparison between rigid and flexible rotors are carried. Finally, the impact of the spatial resolution of the flow is also considered is Section 5.

2 Methodology

2.1 Flow solver

The LES of turbulent flow is performed by solving the incompressible Navier-Stokes equations supplemented by a subgrid scale (SGS) model, using an in-house developed massively parallel code (Duponcheel et al., 2014; Moens et al., 2018). Centered fourth-order finite difference schemes are used for the spatial discretization. The temporal integration is carried using a 2nd order Adams-Bashfort scheme (AB2). The Smagorinsky SGS model (Smagorinsky, 1963) is used, with the asymptotic value of $C_S = 0.027$ corresponding to LES where the grid size is much larger than the Kolmogorov scale (Meneveau and Lund, 1997). For simulation including the ground effect, the wall model developed in Thiry (2017) is used to handle the connection of the LES to the ground. The turbulent inflow consists either in synthetic turbulent fluctuations generated using the Mann algorithm (Mann, 1998) (used in this study for the comparison to the aerodynamic models of OpenFAST) or in a neutral atmospheric boundary layer obtained using a co-simulation (Moens, 2018) (used for the actual study of the loads and wake). In the latter case, a simulation of a half-channel flow is carried with periodic boundary conditions in the streamwise and lateral directions and slip at the top boundary. The flow is driven by a constant pressure gradient, chosen in combination with the ground roughness to obtain the prescribed hub velocity and turbulence intensity (TI). This simulation runs until statistical convergence is reached. Then, it runs concurrently with the main simulation that contains the wind turbines. A vertical plane of velocity is sampled from the channel simulation and is used as inflow for the main simulation, providing a converged flow equivalent to a neutral atmospheric boundary layer. The influence of the wind turbine on the flow is modeled using an actuator line method described hereunder.

https://doi.org/10.5194/wes-2024-19
Preprint. Discussion started: 19 February 2024

eawe european academy of wind energy
Open Access WIND ENERGY SCIENCE DISCUSSIONS

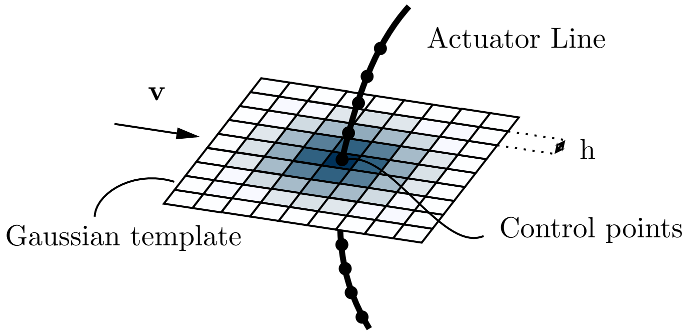

Figure 1. ALM with its associated template with Gaussian weights used for the effective velocity sampling and the forces distribution.

2.2 Actuator Line Method (ALM)

The actuator line method (ALM) consists in representing the effect of the blades on the flow by adding a forcing term to the LES equations (Sorensen and Shen, 2002). An advanced ALM is used, with 2D forces distribution and integral velocity sampling (Jha and Schmitz, 2018; Churchfield et al., 2017). The components of the aerodynamic force acting on each cross-section of the discretized blade are computed using the effective velocity at the control point (corresponding to the aerodynamic center of the local airfoil profile) and the lift and drag coefficients of that airfoil. This effective velocity is obtained by interpolating the velocity at the flow solver grid points to the nodes of a 2D template centered on the control point and lying in the airfoil plane, as depicted on Figure 1. Then, the effective velocity is taken as a weighted average, using Gaussian weights. Here, the Gaussian weights are obtained using a 2D Gaussian kernel of width σ. Its value is taken relatively to the mesh spacing h and is set to $\sigma/h = 2$; similarly to Troldborg (2008). The distribution of the force is also performed in two steps. First, the force evaluated at the blade control point is distributed on the cells of the 2D template using the same Gaussian weights as that used for the velocity. Then, the force on each cell of the template is redistributed on the closest flow grid points using a linear distribution kernel (as this keeps the distribution as local as possible). The position of the control points is also updated to follow the time evolution of the deforming configuration.

For aeroelastic simulations, the accuracy of the loads provided by the ALM is essential as they drive the structural dynamics. However, this accuracy is often questioned, especially at the blade tip, mostly due to the regularization of the forces that reduces the induced velocity. To mitigate this issue, it is either possible to use tip corrections (see (Dağ and Sørensen, 2020; Meyer Forsting et al., 2019; Martínez-Tossas and Meneveau, 2019; Kleine et al., 2023)) or to use regularization kernels that lead to a more accurate prediction of the forces (Caprace et al., 2019; Jha and Schmitz, 2018). The second approach is used here, by using the 2D Gaussian regularization for both the evaluation of the effective velocity and the forces distribution. This leads to a better estimation of the aerodynamic loads, hence much decreasing the need for a tip correction, especially when slender blades are considered. A more detailed description of the used regularization is provided in Trigaux et al. (2022) and its advantages over a 3D distribution are detailed in Caprace et al. (2019).

https://doi.org/10.5194/wes-2024-19
Preprint. Discussion started: 19 February 2024

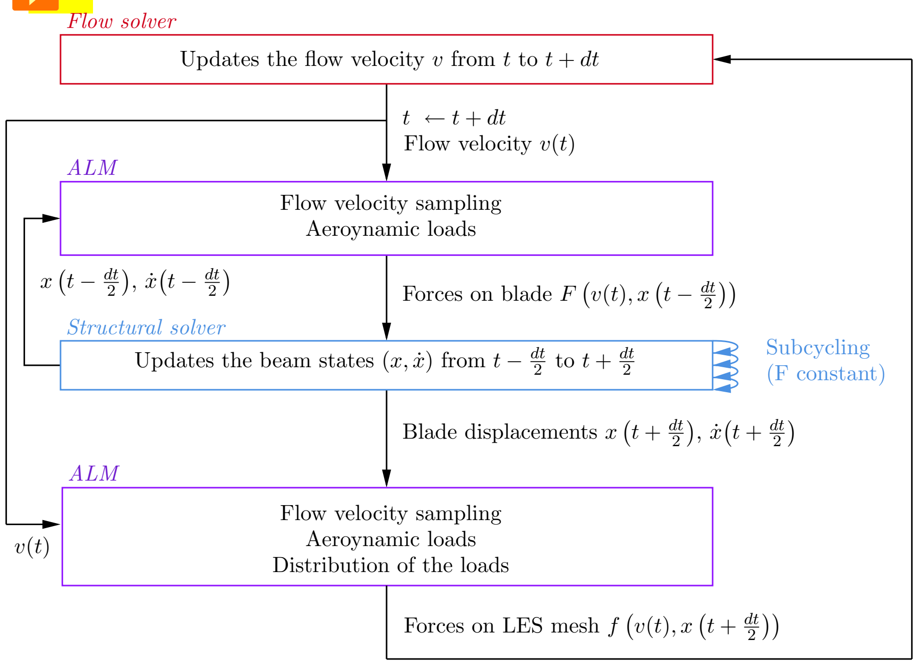

Figure 2. Schematic of the coupling between the flow and structural solver with the ALM as interface.

2.3 Structural solver

115 The structural dynamics of the blades are simulated using the *BeamDyn* module from OpenFAST (Wang et al., 2017). *BeamDyn* implements the nonlinear geometrically exact beam theory, which is particularly suited to study slender blades made of composite materials as it accounts for the large displacements and allows the coupling of degrees of freedom using full 6×6 cross-sectional mass and stiffness matrices. For the considered IEA 15-MW blade, this coupling mainly relates the flapwise and edgewise bending to the twist, which can substantially modify the angle of attack of the blade sections under classical 120 loading conditions. The use of *BeamDyn* is justified by the importance of the non-linear effects over large rotors (Manolas et al., 2015; Panteli et al., 2022). The structural data provided in Gaertner et al. (2020) are used. For this turbine, preliminary analysis indicates that the time-step must be constrained by $dt < 0.005$ seconds to correctly capture the dynamics of the first torsional mode. Each blade of the turbine is represented by one instance of the structural beam solver, for which the kinematics of the blade root is imposed. The simulations presented in this paper all consider a constant rotation speed, which decouples the blade root boundary condition from the other blades and drivetrain dynamics. This allows to use a larger time-step than those typically used in OpenFAST simulations. *BeamDyn* is coupled to the ALM as described in the following section.

https://doi.org/10.5194/wes-2024-19
Preprint. Discussion started: 19 February 2024

eawe european academy of wind energy
Open Access WIND ENERGY SCIENCE DISCUSSIONS

2.4 Coupling

The coupling scheme linking the flow and structural solvers is the 2nd order Improved Serial Staggered (ISS) (Degroote, 2013), which is detailed in Figure 2. This scheme consists in evaluating the flow and the structural models at different time levels. The flow velocity is evaluated at time t and is used by the ALM to evaluate the aerodynamic forces based on the previous structural states $x(t-dt/2)$ (the states include the blade deformation, position and velocity). The structural response to these loads is then integrated in time, using sub-cycling (with constant forces) to meet the structural solver constraints on the time-step. The forces are then reevaluated by the ALM using the updated structural states, and are distributed on the flow mesh according to the deformed configuration.

The computational time required for solving the structural dynamics is much lower than that required by the flow solver. *BeamDyn* is very efficient thanks to the use of high-order spectral finite elements (Sprague and Geers, 2008). When the turbine operates at a constant rotation speed, the time-step also remains relatively large, resulting in fewer necessary sub-steps. Additionally, the structural dynamics of each blade is here solved in parallel, leveraging the multiple CPUs dedicated to the flow solver that would otherwise remain in standby until the completion of the structural computation. As a result, the total overhead generated by the call to the structural solver is less than 5% compared to simulations performed with rigid blades. More details over the implementation of the coupling between the ALM and the structural solver in parallel are provided in appendix A.

The frames of reference in which the blade displacements, loads and wake will be presented are also defined according to Figure 3. The global frame, in which the wake quantities are presented, is located at the tower bottom. The ($\hat{\mathbf{e}}_\mathbf{x}$, $\hat{\mathbf{e}}_\mathbf{y}$, $\hat{\mathbf{e}}_\mathbf{z}$) directions corresponds respectively to the streamwise, vertical and lateral directions. The loads are presented in the blade root frame $\hat{\mathbf{e}}_\mathbf{b}$. Its origin is located at the basis of the blade, and its orientation accounts for the shaft tilt angle, the blade rotation and the cone angle. The displacements are also measured in the blade root frame, and are considered as the variation from the undeflected configuration. The torsion angle is defined along the $\hat{\mathbf{e}}_{\mathbf{y},\mathbf{b}}$ axis, such that a positive value of the angle corresponds to a nose-up rotation of the blade section.

The presented methodology allows to simulate many rotations of wind turbines with flexible blades in LES at a reasonable computational cost (i.e., a few thousands of CPUh for the simulations presented in the next section). In what follows, it is compared to various aerodynamic models of OpenFAST before being applied to assess the effect of the flexibility over the IEA-15 MW turbine.

3 Comparison to the BEM theory and to a free vortex wake model

The methodology developed in the previous section is here tested and compared against the results obtained using different aerodynamic models available in OpenFAST (v3.5.0). OpenFAST is a publicly available modular framework that uses physics-based models to perform aero-servo-elastic simulations of wind turbines under various conditions (Jonkman, 2013). The presented comparison aims at verifying our methodology as well as pointing the limitations of some aerodynamic models for large wind turbines.

https://doi.org/10.5194/wes-2024-19
Preprint. Discussion started: 19 February 2024

Open Access WIND ENERGY SCIENCE DISCUSSIONS

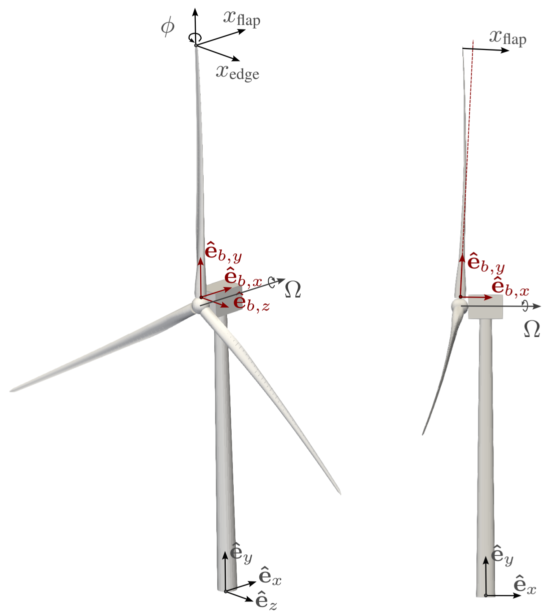

Figure 3. References frames: global frame (black, $\hat{\mathbf{e}}$) and blade root frame (red, $\hat{\mathbf{e}}_b$). The rotor rotation vector Ω and the blade tip displacements (x_{flap}, x_{edge} and ϕ) are also shown. 3D turbine rendering from OpenFAST.

The IEA 15-MW reference wind turbine is here considered with the following parameters. The blades have a length of 117 m and the hub radius is 3 m, leading to a total diameter $D = 240$ m. To avoid tower strike, the blades are pre-bent by 4 m, the shaft is tilted by an angle of $-6°$ and the rotor has a cone angle of $4°$. The gravity loads are also included. All the parameters used for this model are provided in the turbine definition, except from the structural torsional damping factor which was increased to avoid torsional instabilities when the turbine operates in near-rated highly loaded conditions.

The following investigation compares the result obtained using the flexible ALM to those obtained using two aerodynamic models from OpenFAST: the Blade-Element Momentum Theory (BEM) model and a free vortex wake model (cOnvecting LAgrangian Filaments, OLAF) (Jonkman et al., 2015; Shaler et al., 2020). *BeamDyn* is used for the blade structural dynamics in all the considered cases.

3.1 Comparison in uniform flow

The case of a uniform inflow is first considered. The inflow wind speed is set to $U_\infty = 9\,\mathrm{m\,s^{-1}}$, which corresponds to the region of the controller where the optimal tip-speed ratio (TSR) of 9 is maintained. Consequently, the constant turbine rotation speed Ω is set to 6.45 rpm. The ALM and OpenFAST simulations run for 200 seconds, which corresponds to $\simeq 21.5$ rotations, and the results are averaged over the last four rotations. For the ALM simulations, the computational domain size is $12\,D \times 12\,D \times 12\,D$ (in the streamwise, vertical and transverse directions, respectively). The turbine is located at the position $(4\,D, 6\,D, 6\,D)$ to ensure a sufficient distance from the domain boundaries. This way, the blockage ratio is $\simeq 0.5\%$, which allows to compare the

https://doi.org/10.5194/wes-2024-19
Preprint. Discussion started: 19 February 2024

Table 1. Comparison of the time-averaged thrust coefficient (C_T), power coefficient (C_P) and tip deformation predicted by the various methods.

Method		C_T [-]		C_P [-]		Flapwise [m]	Edgewise [m]	Torsion [deg]
Rigid	ALM	0.822		0.532		–	–	–
	OLAF	0.836	(+1.7%)	0.544	(+2.4%)	–	–	–
	BEM	0.804	(-2.1%)	0.488	(-8.2%)	–	–	–
Flexible	ALM	0.743		0.503		11.92	-1.02	-2.82
	OLAF	0.765	(+2.6%)	0.517	(+2.6%)	12.27	-1.08	-2.80
	BEM	0.732	(-1.3%)	0.479	(-4.4%)	11.76	-1.02	-2.83

ALM simulations to the OpenFAST aerodynamic models that do not account for the presence of lateral boundaries. A uniform resolution of 64 flow grid points per diameter is used and the time-step is set to $\simeq 0.025$ s to obtain 360 time-steps per turbine rotation. For the OLAF model, 50 blade nodes are used in the analysis and the time-step is set to 0.155 s, which corresponds to an azimuthal increment $\Delta\theta \simeq 6°$ per time-step, as suggested in the guidelines (Shaler et al., 2020). The circulation on the blade is obtained using the same airfoil polars as that used in the ALM. The near wake consists of 600 vortex panels, which gives a wake length corresponding to 10 rotations. There is no far wake region. The last third of the wake is frozen to mitigate the effect of the wake truncation. The vortex core is regularized using the Vatistas vortex model with the optimized parameters option. The regularization also evolves with time using a viscous diffusion model (here with the parameter $\delta = 1000$). For the BEM, 50 radial locations are used. The Prandtl's tip-loss factor is used to model the tip and the hub losses (Moriarty and Hansen, 2005). The tangential induction is accounted for in the BEM equations, and the effect of the drag term is considered in both the axial and tangential induction. The OpenFAST cases have a very small time-step of 0.0005 s, which is necessary to ensure the convergence of *BeamDyn*. Interested readers can refer to the IEA 15-MW definition that contains example cases with OLAF and the BEM (Gaertner et al., 2020).

A comparison of the rotor thrust and power coefficients predicted by each method is provided in Table 1. For the rigid case, the thrust and power coefficients of the ALM and OLAF match well, whereas the BEM tends to predict a lower power coefficient. For the flexible case, the tip displacement is predicted similarly by all methods. These deflections are particularly significant in the flapwise direction, reaching a value of 12 m at the blade tip, which corresponds to around 10% of the blade length. The torsion angle reaches -2.8° at the tip (corresponding to a nose-down rotation of the airfoil), which also importantly reduces the angle of attack of the blade section, resulting in a noticeable variation of the thrust and power coefficients when accounting for the blade flexibility. Specifically, all methods predict a 9% decrease of the thrust coefficient. The variation of the power coefficient variation is closer to 5% for the ALM and OLAF, whereas the BEM predicts a smaller reduction of 2%. As a result, the difference in power coefficients between the methods is lower when flexibility is considered.

https://doi.org/10.5194/wes-2024-19
Preprint. Discussion started: 19 February 2024

WIND ENERGY SCIENCE DISCUSSIONS

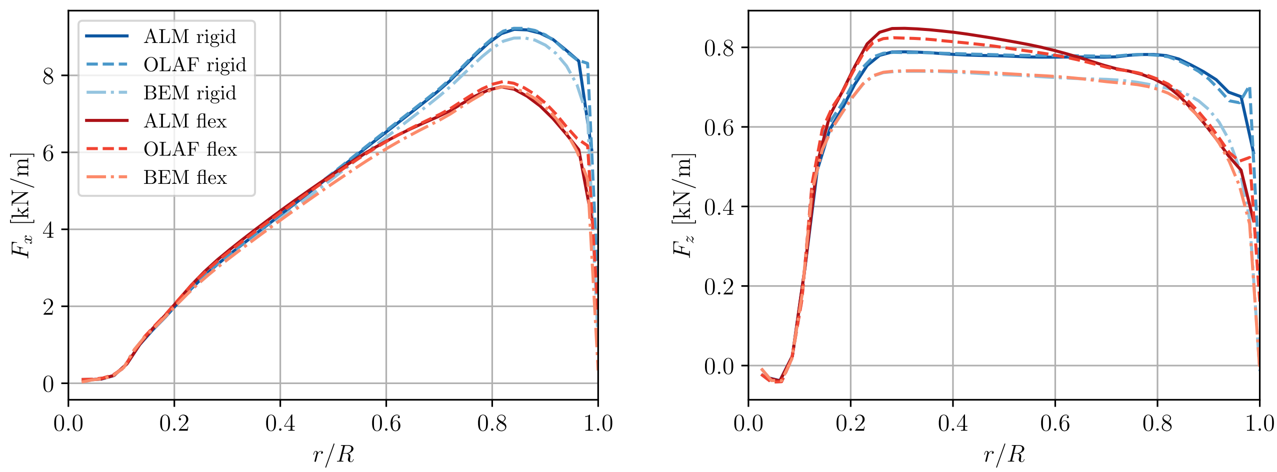

Figure 4. Steady state aerodynamic loads in the blade root frame for the rigid (blue) and flexible (red) cases: ALM (dark solid), free vortex wake model OLAF (dash) and the BEM (light dash-dot) from OpenFAST. Normal (F_x, left) and lateral (F_z, right) forces (relative to the blade root frame).

The aerodynamic forces acting on the rigid and flexible blade are displayed in Figure 4. These forces are expressed in the blade root frame. For the rigid case, the forces obtained using OLAF and the LES using ALM match very well. The only noticeable difference between the two method is the small increase of the forces near the blade tip, which is due to the regularization. To a smaller extend, the ALM also depicts a slight increase of the lateral forces at the tip due to the mollification. The forces distribution predicted by the BEM is lower than for OLAF and the ALM, especially in the edgewise direction. This difference was also observed in other studies (Madsen et al., 2012; Perez-Becker et al., 2020) and can be explained by two factors. High thrust coefficients are somewhat challenging for the BEM as the limits of the validity of the theoretical model are reached, and the empirical Glauert correction is used. On the other hand, the mollification of the ALM and the regularization of the vortex core in OLAF also affects the induction, which can result in slightly higher forces (Shaler et al., 2023).

When flexibility is considered, all methods predict a significant decrease of the loads on the outer part of the blade ($r/R > 0.6$). This decrease is more important for OLAF and the ALM than for the BEM, especially in the edgewise direction. This difference arise from the fact that the BEM predicts less change of the axial induction due to the out-of-plane bending. Conversely, the effect of the torsion angle is captured similarly by all methods, which results in a similar load distribution in the flapwise direction. Additionally, on the inner part of the blade ($r/R < 0.5$), OLAF and the ALM show an increase of the loads. This phenomenon arises from the additional flapwise deformation of the blade that modifies the location of the emission of the tip vortices and was also observed to a smaller extent for the NREL-5 MW turbine (Dose et al., 2018; Trigaux et al., 2022). It is not captured by the BEM as the effect of the blade curvature on its aerodynamics is here not modeled (Fritz et al., 2022; Li et al., 2022). These findings are also consistent with the results predicted by the BEM and blade-resolved URANS simulation

https://doi.org/10.5194/wes-2024-19
Preprint. Discussion started: 19 February 2024

Open Access WIND ENERGY SCIENCE DISCUSSIONS

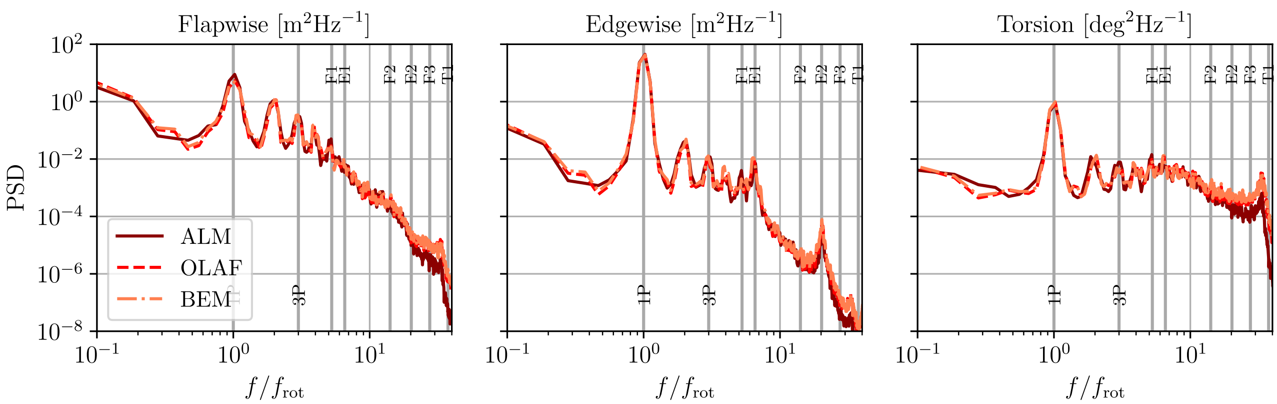

Figure 5. PSD of the tip displacement in the flapwise and edgewise direction and torsional deformation. Comparison between the ALM (dark solid), OLAF (dash) and the BEM (light dash-dot). The vertical lines denote the main frequencies of the system (1P and 3P), and the flapwise (F), edgewise (E) and torsional (T) natural frequencies.

for the DTU-10 MW turbine presented in Sayed et al. (2019). This highlights the importance of using higher fidelity methods when the aeroelasticity of large rotors is considered, also for steady loads such as those presented in this section.

3.2 Comparison in turbulent flow

To verify the dynamic response of the structure under unsteady loads, a comparison between our framework and OpenFAST is also carried with a turbulent inflow. The latter consists in the superposition of a uniform flow with U=9 $\mathrm{m\,s^{-1}}$ and of a turbulent field generated using the Mann algorithm (Mann, 1998). The parameters of the turbulent field are the integral length scale, here set to $L = 88.5$ m, the anisotropy factor $\Gamma = 3.9$, and the turbulence intensity, set to $TI = 6\%$. The turbulent fluctuations are generated in a 3D domain of size $8\,D \times 2\,D \times 2\,D$, with a spatial discretization of 32 pts/D. In OpenFAST, the turbulent fluctuations are directly interpolated from the 3D domain to the turbine blade nodes and added to the upstream velocity value. In the case of the ALM, the turbulent fluctuations are interpolated to the inflow plane and are then convected to the turbine location. The OpenFAST cases are kept identical to the cases with a uniform inflow. Only the time-step at which OLAF emits a new panel is decreased to 0.1 s to better account for the turbulent fluctuations. The ALM case also remains identical, except that the distance between the turbine and the inflow plane is reduced to $2\,D$ to reduce the variation of the turbulent fluctuations that occurs during their convection from the inflow to the turbine. The cases run for 400 s to converge the statistics.

The dynamic structural deformation of the blade is considered for this comparison to assess that the flexible ALM correctly captures the variations of the displacements at the relevant frequencies. Figure 5 depicts the power spectral density (PSD) of the tip displacement for the flapwise and edgewise translations, and for the torsion angle. The PSDs are computed using the Welch algorithm with segments of duration equal to 50 s that overlaps by half their length (Welch, 1967). The blade natural frequencies are also depicted. These were obtained using the mass and stiffness matrices provided by *BeamDyn* in the rotating

https://doi.org/10.5194/wes-2024-19
Preprint. Discussion started: 19 February 2024

undeformed configuration, without accounting for the coupling with the aerodynamic loads. A very good agreement is observed between OpenFAST and the ALM. All the methods predict the same magnitude for the peak occurring at the 1P frequency for all three components. Additionally, the peaks of displacement occurring at the edgewise natural frequencies (E1 and E2) are present and reach the same value for all three solvers. The structural response close to the first torsional frequency (T1) is also similar for all methods. All three solvers predict a similar decrease of the frequency at which this peak arises compared to the T1 frequency. This shift is due to the coupling between the aerodynamic forces (that increase linearly with the angle of attack) and the torsion angle. The amplitude of the peak is however slightly smaller for the ALM. This can be attributed to the lower amplitude of the high frequency fluctuations that are close to the cut-off frequency of the present LES. Additionally, the ALM uses the integral velocity sampling, which leads to some smoothing of the fluctuations during the sampling step. Some additional differences in the lower frequency part of the spectrum are related to changes in the turbulent fluctuations during their convection from the inflow to the turbine location (Mann et al., 2018).

4 Investigation of rigid and flexible rotors in atmospheric conditions

In this section, rigid and flexible rotors are studied with a sheared turbulent wind as inflow, to evaluate the effects of the unsteady aeroelastic effects on the aerodynamic loads and on the wake. To that purpose, the numerical set up consists of a domain of size $12\,D \times 4\,D \times 4\,D$, with a spatial resolution of 64 grid points per D. The turbine location is $(2D, 150m, 2D)$. To ensure a valid comparison between the rigid and flexible cases, the rotation speed is imposed at the blade root to $\Omega = 0.75\ \mathrm{rad\,s^{-1}}$, which corresponds to the design TSR of 9. The time increment of the flow simulation is set to obtain 360 time-steps per turbine rotation. Additionally, there are 4 structural sub-steps per flow time-steps. A total of 200 rotations is simulated for each case, which corresponds to a physical time of 1675 seconds.

The inflow is a neutral ABL generated using the co-simulation technique (as described in Section 2.1). The numerical setup is described in details in Appendix B. It was designed so as to obtain a time-averaged velocity of $U_{hub} = 10\ \mathrm{m\,s^{-1}}$ at hub height, and with a TI close to 5%. The obtained profiles of mean velocity and turbulence intensity are also provided in the Appendix, together with the methodology used to estimate the integral length scales, obtained as 106 m in the streamwise direction and 89.5 m in the lateral direction.

Three cases are compared in this section. The first case is the “rigid undeformed” rotor, thus with the upwind pre-bend of the blades. The second case is the flexible rotor, modeled using the flexible ALM that dynamically deforms based on the aerodynamic loads. A third case considers a rigid rotor that includes the mean deformation of the blades, noted as the “rigid deformed” case. The deformed geometry was obtained by time-averaging the structural displacements obtained in the second case. This allows to isolate the effect of the time-varying response of the blade on the rotor dynamics and wake.

This analysis is structured in three parts. First, the displacements of the blades are considered. Then, the distribution of the loads as well as their variation is presented. Understanding these aspects allows to explain the differences observed in the wake, which are presented in the last part of the analysis.

https://doi.org/10.5194/wes-2024-19
Preprint. Discussion started: 19 February 2024

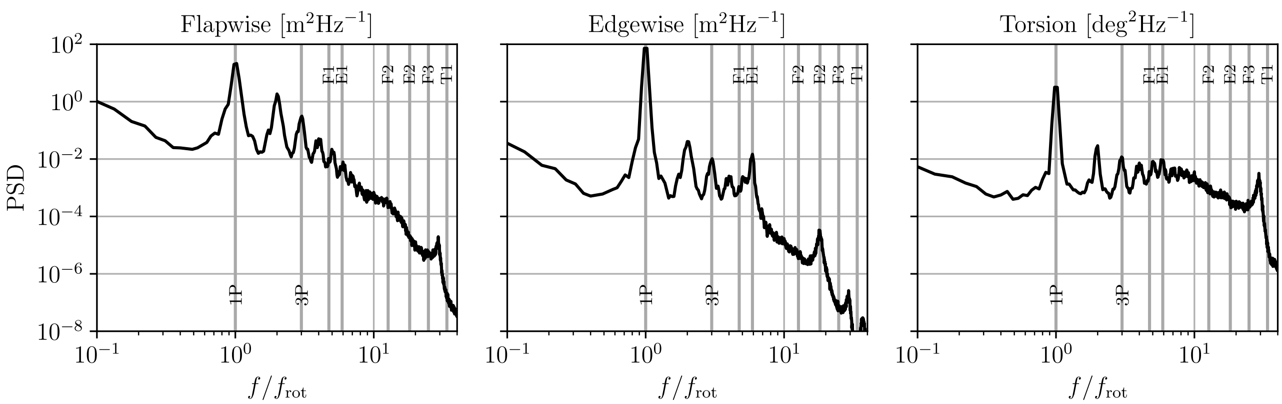

Figure 6. PSD of the tip displacement in the flapwise and edgewise direction and of the tip torsion angle. The vertical lines denote the main frequencies of the system (1P and 3P), and the flapwise (F), edgewise (E) and torsional (T) natural frequencies.

4.1 Structural displacements

The PSD of the displacements is first considered in figure 6. In this section, the presented statistics of the blade displacements and loads are computed using the last 180 rotations of the simulations (the 20 first rotations are discarded as the wake induction is not yet converged). The presented PSDs are computed using the Welch algorithm. The time-series are divided in sub-segments of length corresponding to 22.5 rotations that overlaps by half their length, resulting in a total of 15 segments. The PSDs are also computed for each blade and then averaged, resulting in smooth spectra. For all the components of the displacement, the 1P frequency is the most noticeable. In the flapwise direction, the 1P frequency is excited by the rotation of the blade in the mean shear and in the spatially coherent turbulent structures. For the edgewise direction, the excitation of the 1P frequency is mostly attributed to the gravity. In this direction, the peak at 1P is much more pronounced than the rest of the spectrum, indicating the dominance of the gravity over the aerodynamic loads. In the torsional direction, the peak at 1P is due to the coupling with the translational degrees of freedom. The harmonics of the rotation frequency are also important in all spectra. Concerning the blade structural frequencies, their excitation depends on the considered component. In the flapwise direction, the PSD exhibits no particular excitation at the flapwise (F1, F2 or F3) frequencies. Only a small peak is visible near the torsional frequency. The absence of a peak is explained by the high aerodynamic damping of the flapwise mode. This damping is due to fact that the blade flapwise displacement decreases the apparent streamwise velocity on the blade section, hence decreasing the angle of attack and the loads.On the contrary, in the edgewise direction, distinguishable peaks of displacement occur at the edgewise natural frequencies (E1, E2) and close to the torsional frequency (T1). This is a result of the small aerodynamic damping in this direction, yet the amplitude of the peaks remains small compared to the one occurring at 1P. For the torsional direction, a peak occurs slightly below the T1 frequency, as observed in Section 3.2.

https://doi.org/10.5194/wes-2024-19
Preprint. Discussion started: 19 February 2024

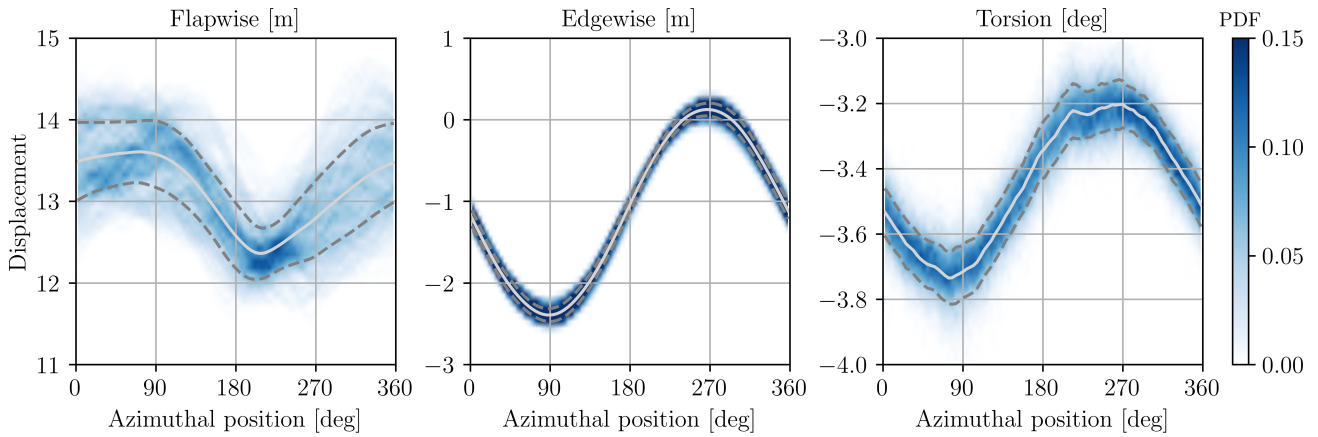

Figure 7. Tip displacement: mean (solid), standard deviation (dash) and values encountered over the turbine rotations (blue, approximating a PDF) as a function of the blade azimuthal angle (as measured from the blade upwards position).

It is also interesting to consider the general shape of the displacements spectra. In the flapwise direction, the PSD follows a general downward slope that is constant through most of the spectrum. In the edgewise direction, a similar trend is noticeable before the 1P frequency and between the E1 and T1 frequencies. However, for the first harmonics of 1P, the general trend of the PSD remains constant. For the torsional direction, the general shape of the spectrum remains constant across the frequencies. Consequently, in this direction, some non-negligible high frequency modes are observed additionally to the rotation frequency.

As the rotational frequency appears as predominant, it is interesting to investigate the variation of the displacements along one rotation. The mean displacement and standard deviation are represented in Figure 7 as function of the azimuthal angle (zero representing the blade pointing upwards). The values measured at each angle and over the simulated turbine rotations are also plotted; for each angle, they can be viewed as an approximation of the probability density function (PDF). In the flapwise direction, the minimal blade displacement is reached a few degrees after the blade downwards position. In this region, the PDF also has the smallest spread. Interestingly, the maximal mean flapwise displacement is not reached at the blade upwards position (i.e., 0°), where the flow velocity is maximal, but is rather constant from 0° to 90°. The PDF also exhibits a larger spread when the blade is in the upper half region (i.e., between 270° and 90°). Overall, the flapwise deformation varies significantly along the rotation, oscillating between 12.4 m and 13.6 m, primarily due to the mean shear of the flow. The PDF also reveals large variations around the mean displacement, attributable to the turbulent fluctuations. On the contrary, the edgewise displacement present a nearly perfect sinusoidal variation that is consistent with the gravity loads. The spread around the mean is also very limited, as the variation of the aerodynamic loads is small compared to that of the gravity. The torsional deformation follows the same phase as the edgewise displacement. This is due to the effect of the gravity loads and of the flapwise deformation, that generates a torsion moment on the structural reference axis. Consequently, the torsion angle differs between the left and right part of the rotor, which can lead to some additional load imbalance. The PDF also presents a larger width than for the edgewise displacement, as a result of the higher sensitivity to the turbulent fluctuations.

https://doi.org/10.5194/wes-2024-19
Preprint. Discussion started: 19 February 2024

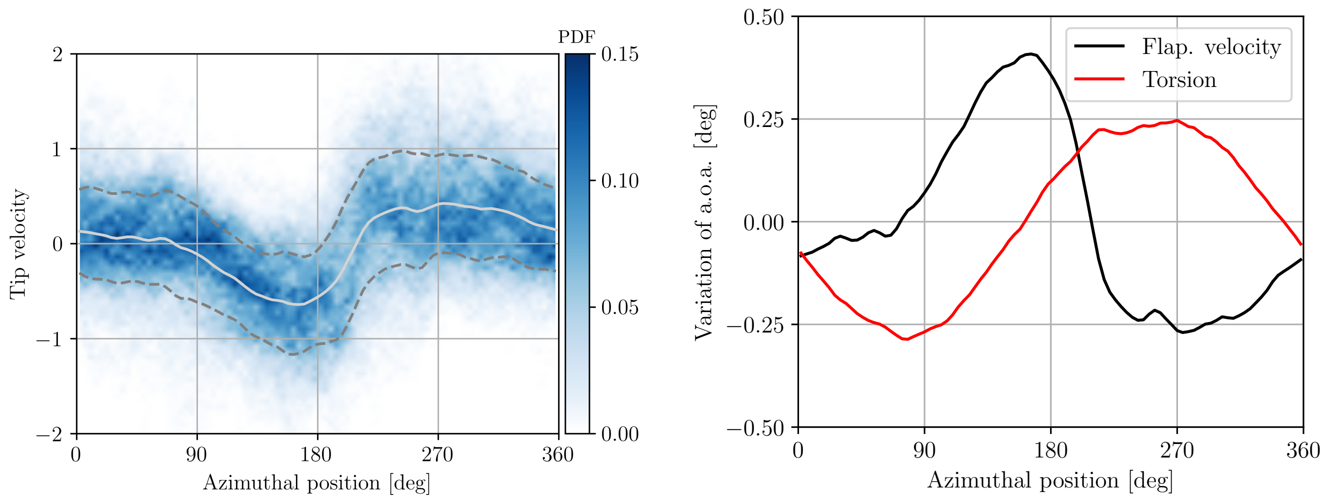

Figure 8. Left: flapwise structural velocity at the tip: mean (solid), standard deviation (dash) and values encountered over the turbine rotations (blue, approximating a PDF) as a function of the blade azimuthal angle. Right: comparison of the impact of the flapwise velocity $-v_{\mathrm{struct},x}/(\Omega r)$ and of the torsion angle $(\phi_{\mathrm{struct},y} - \bar{\phi}_{\mathrm{struct},y})$ on the angle of attack.

The flapwise structural velocity is also considered as it affects substantially the angle of attack and hence the aerodynamic forces. In fact, the angle of attack α of a section of the blade is given by

$$\alpha = \arctan\left(\frac{(v_x - v_{\mathrm{struct},x})}{(v_{\mathrm{struct},z} - v_z)}\right) + \phi_{struct,y} + \beta,$$

where v_x, v_z are the local flow velocity in the x (streamwise) and z (azimuthal) directions, $v_{\mathrm{struct},x}$, $v_{\mathrm{struct},z}$ are the local structural velocity in these directions, $\phi_{\mathrm{struct},y}$ is the local torsion angle and β is the local twist angle. In general, the structural velocity in the z direction mostly consists of the rotational velocity Ωr, and the flow velocity is also negligible relatively to that, leading to $(v_{\mathrm{struct},z} - v_z) \simeq \Omega r$. Additionally, since the normal velocity is also much smaller than the rotational velocity, $\arctan((v_x - v_{\mathrm{struct},x})/(\Omega r)) \simeq (v_x - v_{\mathrm{struct},x})/(\Omega r)$. As a result, the expression for the angle of attack is simplified to

$$\alpha \simeq \frac{(v_x - v_{\mathrm{struct},x})}{(\Omega r)} + \phi_{struct,y} + \beta.$$

Consequently, the ratio $v_{\mathrm{struct},x}/(\Omega r)$ has an effect on the angle of attack that is similar to that of the torsion angle. Figure 8 shows the mean flapwise velocity $v_{\mathrm{struct},x}$ has a function of the blade azimuthal angle and the probability density function for each angle. The maximal positive velocity is 0.4 $\mathrm{m\,s^{-1}}$ and is reached in the left region of the rotor. The minimal velocity is -0.7 $\mathrm{m\,s^{-1}}$ and is reached when the blade is pointing downwards. A large variation of the velocity occurs around the blade downwards position which is attributed to the high mean vertical shear in the lower region of the rotor. The PDF of the flapwise velocity is also quite large around the mean, due to the turbulent fluctuations of the velocity. The figure also shows the contribution of the flapwise velocity $(-v_{\mathrm{struct},x}/(\Omega r))$ to the variation of the angle of attack at the tip along a rotation. It is compared to the contribution of the torsional angle $(\phi_{\mathrm{struct},y} - \bar{\phi}_{\mathrm{struct},y})$. The two effects are similar in magnitude, and

https://doi.org/10.5194/wes-2024-19
Preprint. Discussion started: 19 February 2024

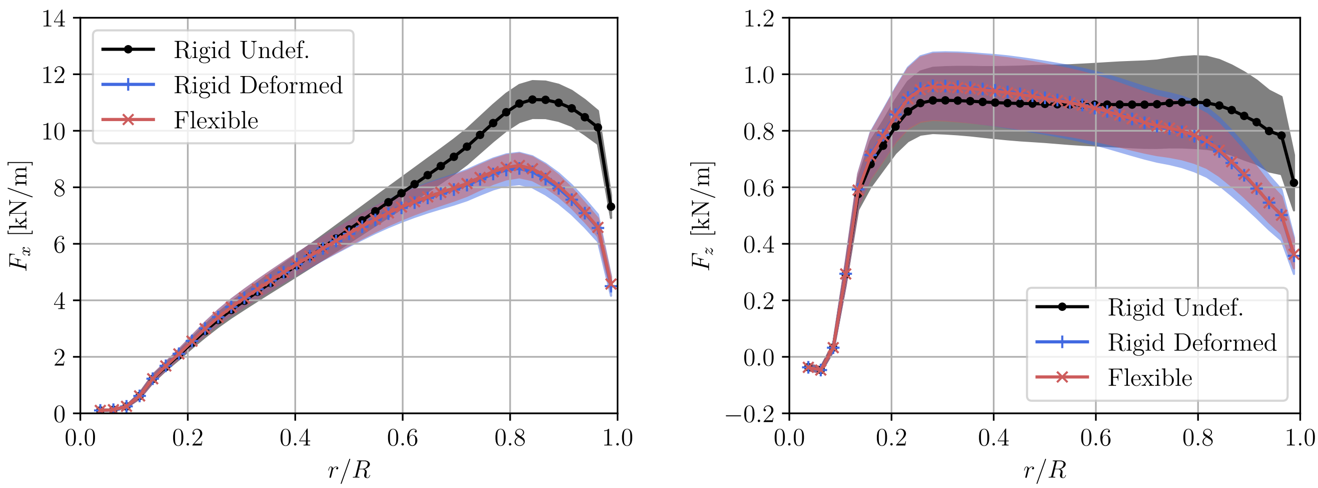

Figure 9. Distribution of the aerodynamic loads along the blade span for the rigid undeformed (black), rigid deformed (blue) and flexible (red) cases. The shaded area represents the standard deviation.

can result in a small variation of the angle of attack up to 0.4°. Their phase is shifted by a quarter of rotation, as the effect on the flapwise velocity mostly depends on the vertical shear, whereas the variation of the torsion follows the same phase as the edgewise displacements (and hence the gravity loads).

These displacements are not without consequences over the loads acting on the turbine, which will be presented in the next section.

4.2 Comparison of the blade loads

This section presents a comparison of the loads obtained with the flexible and rigid rotors. The focus is here set on the blade loads, presenting both the aerodynamic loads, due to their impact on the wake, and the structural loads, due to their effect on the structural integrity. This choice also follows the decision to maintain a constant rotation speed, primarily to facilitate the comparison between the wakes. In real-world conditions, the turbine controller adjusts the rotation speed and the blade pitch angle, and the three blades are dynamically coupled by their rigid connection with the turbine shaft, which modifies the resulting rotor loads, especially the rotor torque. To assess the impact of these changes, the simulations were also conducted with the controller. The loads and displacements of the individual blades were not noticeably affected, and neither was the wake. However, the spectrum of the rotor torque was modified due to the coupling between the blades and the generator. Consequently, we chose to present the simulation at constant rotation speed and to focus on the individual blade dynamics and on the wake, which were confirmed to remain mostly unaffected by the controller.

The mean load distribution along the blade, depicted for each case in Figure 9, is first examined. The load distribution on the undeformed rotor clearly differs from that of the two cases that include the deformation. In particular, a significant reduction of the mean loads and of their standard deviation is induced by the structural displacement on the outer part of the blade.

https://doi.org/10.5194/wes-2024-19
Preprint. Discussion started: 19 February 2024

WIND ENERGY SCIENCE DISCUSSIONS

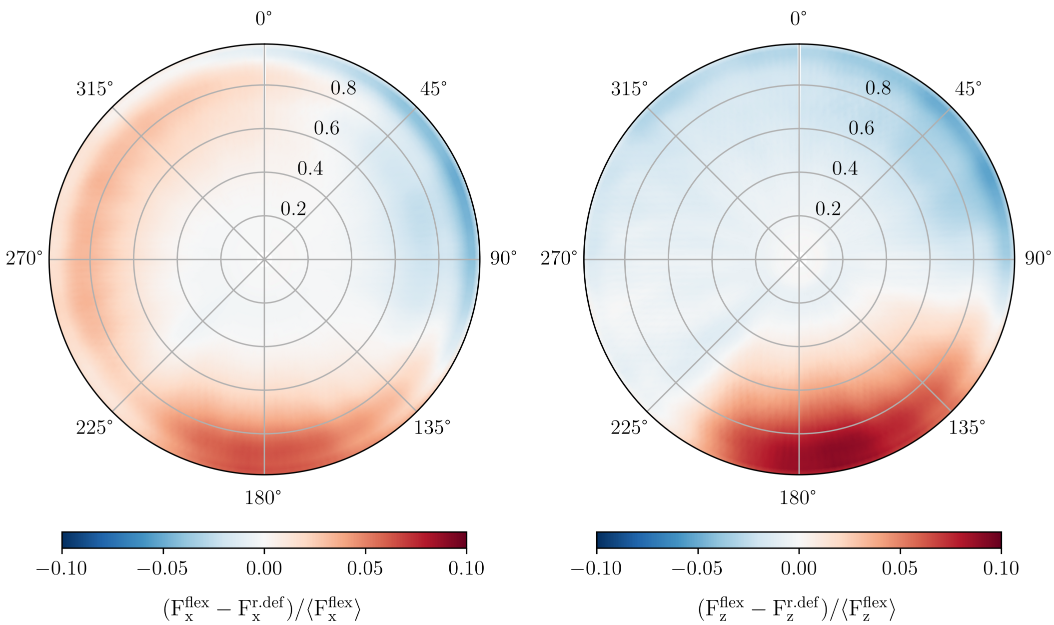

Figure 10. Difference between the aerodynamic force distribution of the flexible case (F^{flex}) and of the rigid deformed case ($F^{\text{r.def}}$) on the rotor plane (front view), normalized by the mean force on the rotor. Left: flapwise forces; right: edgewise forces.

This results in a substantial reduction of the power and thrust coefficients. The thrust coefficient is reduced by $\simeq 14\%$, going from $C_T = 0.80$ for the undeformed rotor to $C_T = 0.69$ for the deformed cases. Similarly, the power coefficient is reduced by 10%, from $C_P = 0.50$ to $C_P = 0.45$. As anticipated, the rigid deformed and flexible cases exhibit a nearly identical mean forces distribution. However, in the flexible case, the standard deviation presents a slight reduction attributable to the additional compliance of the blade.

Although the radial distribution of the forces is the same for the rigid deformed and flexible cases, their distribution over the rotor plane varies. Figure 10 depicts the difference between the forces distribution of the two cases. There is a notable difference at the bottom of the rotor in both the flapwise and edgewise directions. In this region, the flexible rotor undergoes more forces, due to the reduced flapwise deflection, and the important upstream blade velocity that increases the angle of attack as observed in figure 8. In the normal direction, there is also a clear asymmetry between the left and right plane of the rotor. The flexible rotor presents higher forces compared to the rigid ones on the left part of the plane, due to the smaller torsion angle on this side. This asymmetry is not visible in the edgewise direction. The observed differences reach a maximum of around 10% on the lower part of the rotor plane, which will also result in a difference of the mean velocity deficit in the near wake, as discussed in the next section.

Figure 11 presents the PSD of the blade root moment in the two main directions. The spectra are given for the aerodynamic forces and for the elastic structural response (which includes the inertia, the centrifugal and gravitational forces). Considering first the aerodynamic forces, one observes that the rotation frequency is still the most important component. The amplitude

https://doi.org/10.5194/wes-2024-19
Preprint. Discussion started: 19 February 2024

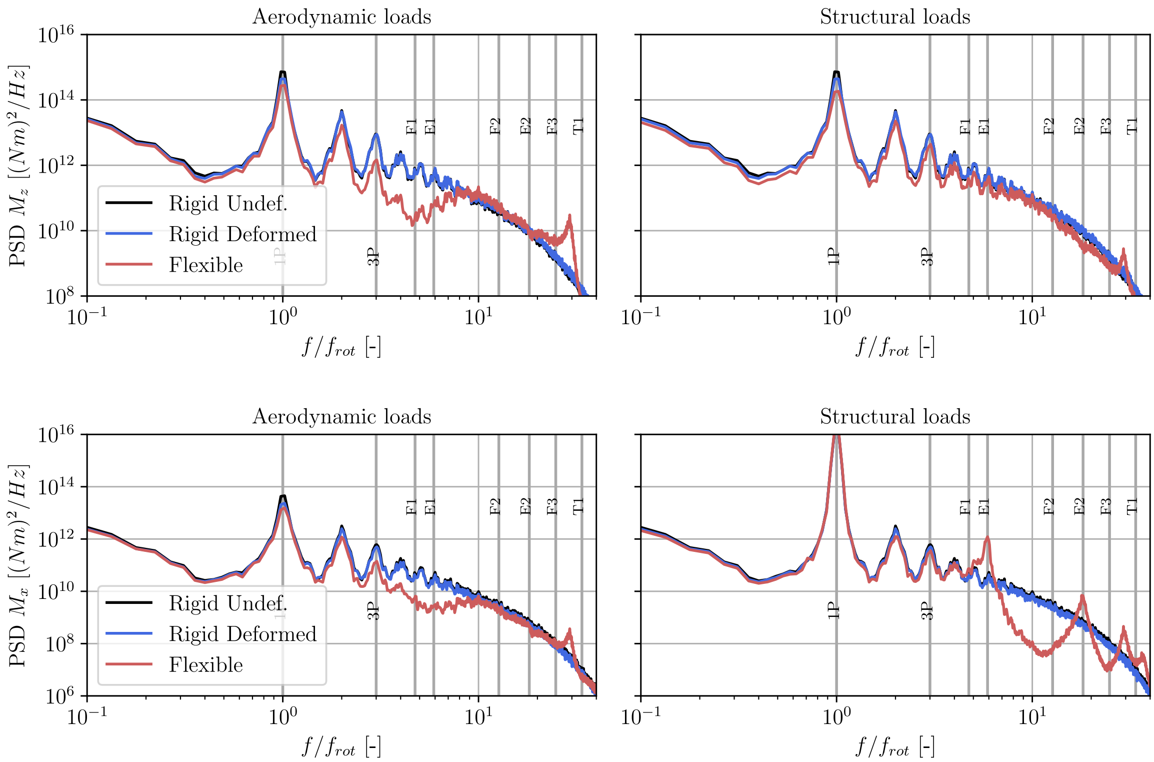

Figure 11. PSD of the blade root moment due to the flapwise forces (M_z, top) and edgewise forces (M_x, bottom). Left: PSD of the moment of the aerodynamic loads; right: PSD of the structural root moment. Comparison between the rigid undeformed (black), rigid deformed (blue) and flexible (red) cases.

of the PSD at that frequency differs slightly between the cases, the rigid undeformed case having the highest value and the flexible case the lowest. Large differences also appear close to the natural frequencies. The PSD is much lower close to the main bending frequencies (F1, E1), due to the dynamic response of the blade. In fact, at these frequencies, the blade responds importantly to the variations of the forces and the resulting structural bending tends to smooth these changes. There is also a noticeable increase at the torsional frequency (close to T1) due to the subsequent modification of the angle of attack of the blade. The structural moment does not exhibit a decrease at the bending frequency, as the lower aerodynamic forces are compensated by the inertial loads. In the flapwise direction, the spectrum of this moment is in general slightly smaller in the flexible case. There are also no specific peaks at the natural frequencies due to the high aerodynamic damping in this direction. On the contrary, the edgewise root moment presents high peaks close to its natural frequencies. In this direction, the value of the PSD at the 1P frequency is also much higher than that of the aerodynamic loads, illustrating the importance of the gravity loads. The modification of the spectrum of the root moment can have a direct impact on the lifetime of the turbine and the

https://doi.org/10.5194/wes-2024-19
Preprint. Discussion started: 19 February 2024

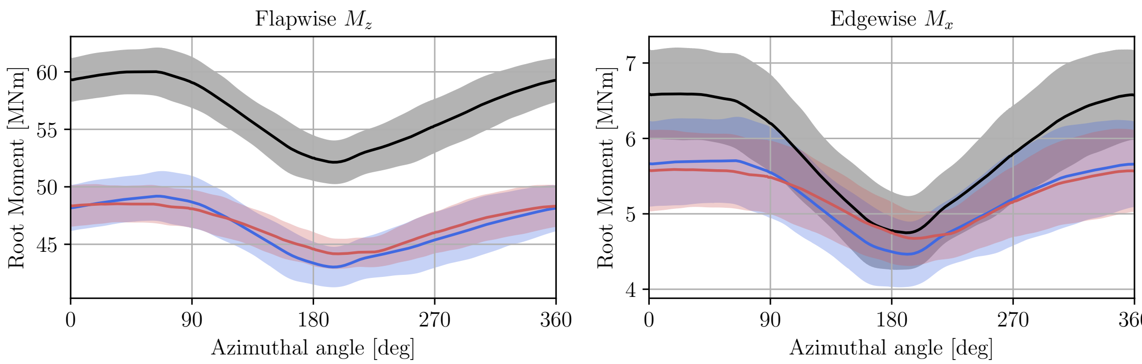

Figure 12. Blade root moment of the aerodynamic forces as a function of the azimuthal angle, and averaged over the turbine rotations: mean value (solid line) and standard deviation (shaded area). Comparison between the rigid undeformed (black), rigid deformed (blue) and flexible (red) cases.

damage equivalent load calculations, as also obtained in Hodgson et al. (2021). It is therefore necessary to consider dynamic models when assessing the structural integrity of the rotor.

Similarly as for the displacement, the variation of the blade root moment of the aerodynamic forces along the rotation is further investigated, as the 1P frequency was shown to be the most significant. The latter is represented in figure 12. The aerodynamic forces are considered instead of the structural response to remove the influence of the gravity, which would be dominant on the edgewise moment.

The mean flapwise moment acting on the rigid turbine is 21% higher than that obtained in the cases that include the deformation, which have a comparable mean value. The amplitude of the deviation along the rotation, defined as $(M_{\text{max}} - M_{\text{min}})/M_{\text{mean}}$, is however similar in both rigid cases (14.0% for the rigid undeformed case and 13.2% for the rigid deformed case). This deviation is reduced to 9.3% in the flexible case, mostly due to a higher minimal value when the blade is in its downwards position. In the edgewise direction, the mean value of the root moment is 12% higher in the rigid undeformed case. The deviation is 31.5% in this case, compared to 23.7% in the rigid deformed case and 17.5% in the flexible case.

Interestingly, there is also a noticeable phase lag between the rigid and the flexible cases. Whereas the rigid case predicts a minimal moment at around $\theta = 195°$, the flexible case predicts a minimum at $\theta = 215°$. This phase lag also applies to the rotor torque and ultimately to the power. It could also have an effect on load alleviation control strategies that uses the root bending moment as input, such as individual pitch control.

4.3 Impact on the turbine wake

In this section, the impact of the flexibility over the wake is considered. The wake can be affected in two ways. Firstly, the displacements of the blade described in Section 4.1 affect the location of the emission of the tip vortices. Specifically, the tip vortices are generated further downstream due to the flapwise bending, and the flexibility affects the distance between

https://doi.org/10.5194/wes-2024-19
Preprint. Discussion started: 19 February 2024

WIND ENERGY SCIENCE DISCUSSIONS

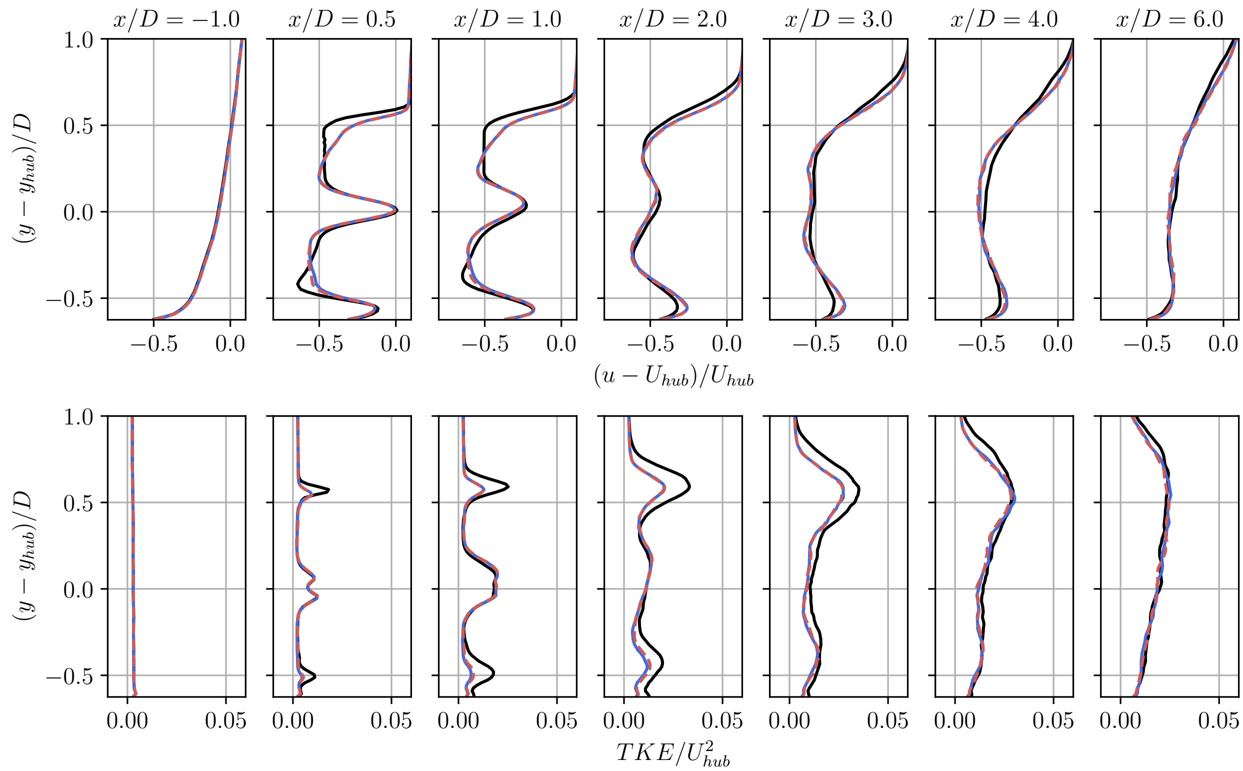

Figure 13. Profiles of mean velocity deficit (top) and turbulent kinetic energy (bottom) in the near wake of the turbine at various downstream locations: rigid undeformed (solid black), rigid deformed (solid blue) and flexible (dash red) cases.

individual tip vortices, potentially modifying their interaction. Secondly, the variation of the loads described in Section 4.2 affects the mean velocity deficit and the magnitude of the tip vortices. This section aims at understanding whether these effects have a significant impact over the wake, its stability and the resulting velocity deficit.

The wake statistics are first considered. The statistics are computed over the last 150 rotations, to ensure that the wake is developed up to the end of the computational domain before averaging. This window of averaging is slightly under 4 convective times. Figure 13 illustrates the time-averaged velocity deficit and turbulent kinetic energy (TKE) profiles. The differences between the profiles of the mean velocity deficit are comparable to the changes of the mean loads distribution. Behind the tip of the turbine, the deficit is more pronounced in the rigid undeformed case compared to the deformed and flexible cases. Additionally, there is a steeper gradient of mean velocity behind the tip in this case. The TKE is also noticeably higher in the near tip region, which results in a faster turbulent diffusion of the wake. For the rigid undeformed case, the velocity deficit observed 3 and $4D$ behind the turbine is smaller but more diffuse than in the deformed cases. In the far wake ($6D$ behind the rotor), the velocity deficit and TKE profiles are almost equivalent. The time-averaged velocity deficit and TKE are very similar

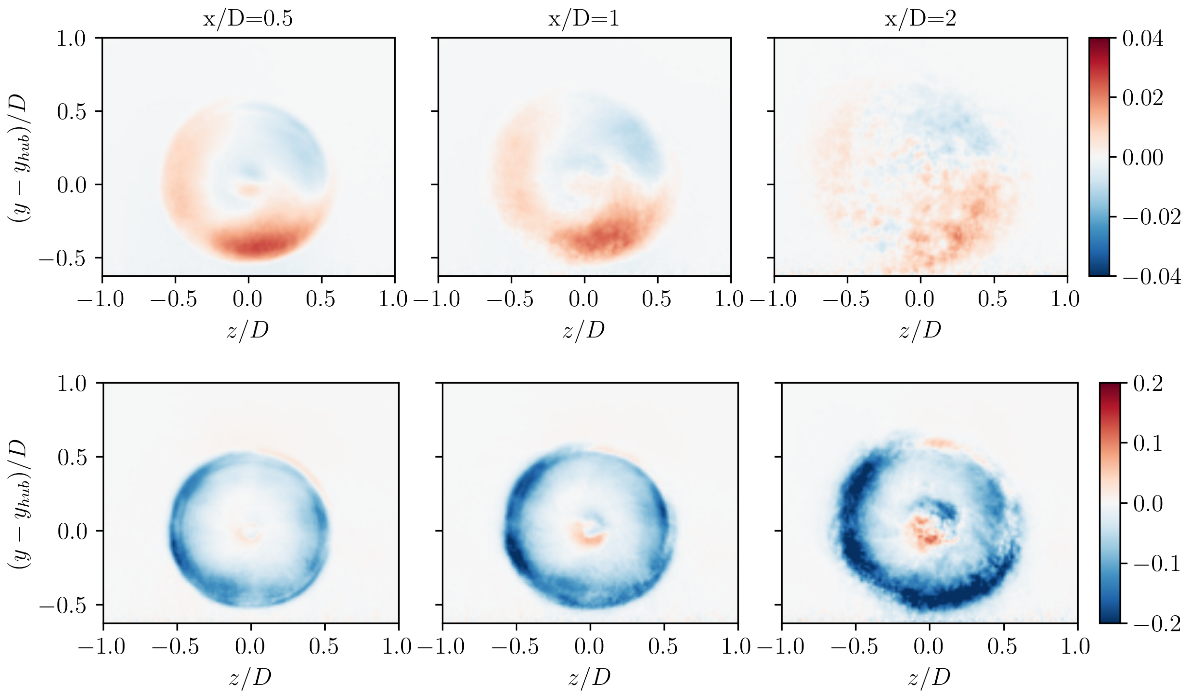

Figure 14. Difference of the mean velocity field (top, $(u_{\mathrm{r.def}} - u_{\mathrm{flex}})/U_{\mathrm{hub}}$) and TKE (bottom, $(\mathrm{TKE}_{\mathrm{r.def}} - \mathrm{TKE}_{\mathrm{flex}})/\mathrm{TKE}_{\mathrm{hub}}$) between the rigid deformed and the flexible cases over vertical planes at several locations behind the rotor.

between the rigid deformed and flexible cases, which indicates that the unsteady variations around the mean deformation have a limited effect on the time-averaged wake statistics.

Some differences between the near wake of the rigid deformed and flexible cases can nevertheless still be observed. Figure 14 presents the difference in mean velocity and TKE over vertical planes behind the rotor. For the mean velocity, the difference of mean velocity behind the rotor ($x/D = 0.5$) is very close to that observed for the blade normal forces on the rotor area (see Figure 10). The small changes in the local thrust result in differences in mean velocity deficit that reach up to 2.5% of the upstream velocity. The most substantial difference occurs behind the bottom of the rotor, where the velocity is significantly higher behind the rigid deformed turbine than behind the flexible turbine. Noticeable differences also exist behind the left and right part of the rotor. At a distance $x/D = 2$, these differences start to vanish due to the wake destabilization that increases the turbulent mixing. The TKE exhibits a different behavior, as it is globally lower in the rigid case compared to the flexible case. The largest differences are observed for $\theta = 90°$ and 270°, which also correspond to the angle with the highest variance of flapwise and torsional displacements. The increase of the TKE in the flexible case is attributed to the unsteady variations of the loads and position that further contributes to the fluctuations in the flow. However, these fluctuations remain moderate compared to the incoming turbulence of the wind, and therefore have a limited impact on the wake behavior.

https://doi.org/10.5194/wes-2024-19
Preprint. Discussion started: 19 February 2024

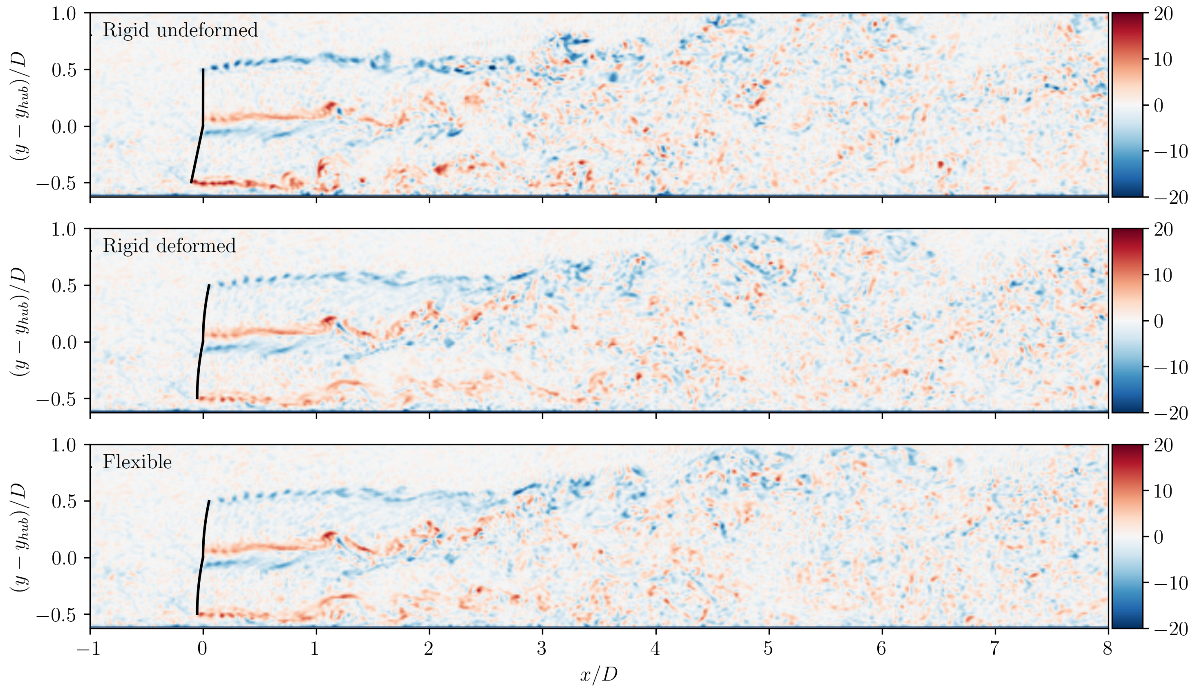

Figure 15. Snapshot of an instantaneous out-of-plane vorticity field ($\omega_z D/U_{hub}$) in the wake of the turbine for the rigid (top), deformed (middle) and flexible (bottom) cases. The inflow is identical for each case.

A snapshot of an instantaneous out-of-plane vorticity field behind the rotor is depicted in Figure 15 on a vertical plane. We stress that the turbulent inflow (furnished by the co-simulation of the ABL) is at exactly the same time t for the 3 cases (i.e., it is synchronized); which allows to compare fine details in the wake. The magnitude of the tip vortices behind the rigid rotors is significantly higher for the rigid undeformed rotor. This results from the higher gradient of the forces observed in the near tip region for the undeformed blades. Additionally, these tip vortices are emitted further upstream compared to those of the deformed cases. As a result, the destabilization of the wake occurs at a smaller distance from the rotor. The rigid deformed and the flexible cases exhibit very similar vortical structures, even in the details. The wakes are almost identical, which further confirms the minimal influence of the unsteady fluctuations of the blade deformations around their mean deformation.

This analysis shows the necessity to include the mean deformation to accurately capture the near wake, but also predicts a minimal effect of the unsteady variations of the displacements and loads around their mean. The spatial resolution of the presented simulations is 64 pts/D, corresponding to 3.75 m, which is larger than the variation of the displacements along the mean deformed configuration. To further assess the impact of the small variations, it is important to verify that the resolution of the flow simulations is sufficient. The next section therefore assesses the effect of the spatial resolution over the loads and near wake dynamics.

https://doi.org/10.5194/wes-2024-19
Preprint. Discussion started: 19 February 2024

WIND ENERGY SCIENCE DISCUSSIONS

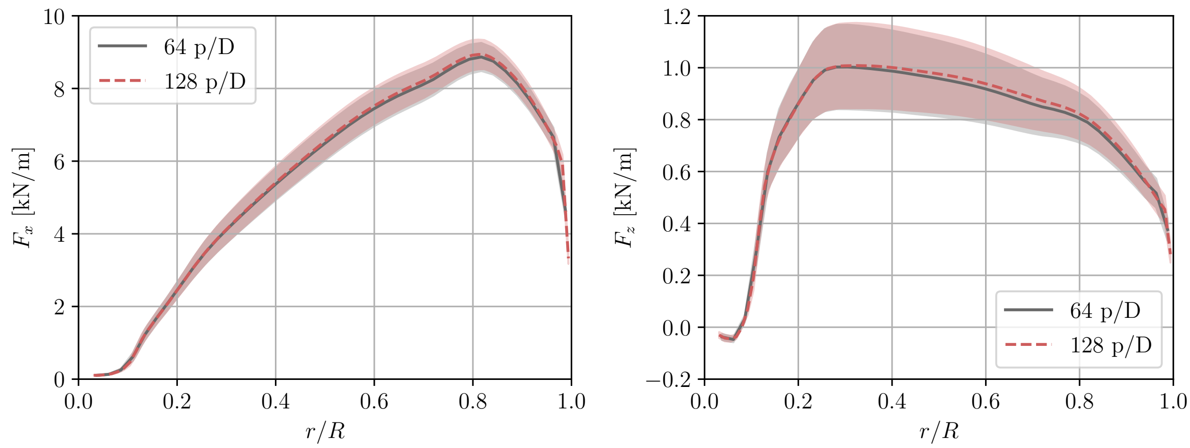

Figure 16. Distribution of the aerodynamic loads along the blade span for the initial resolution (gray) and the increased resolution (red). The shaded area represents the standard deviation.

5 Investigation of the impact of the spatial resolution

In this section, the results obtained with a spatial resolution of 64 grid points per diameter are compared to those of a higher resolution simulation to assess whether the small deviations of loads and displacement around the mean are sufficiently resolved. The case of a flexible rotor is therefore reconsidered with a grid resolution twice as fine, corresponding to 128 grid points per D. The time-step is also divided by two to maintain the CFL constant. The mollification of the ALM forces is maintained constant relatively to the grid size (i.e., $\sigma/h = 2$), and is thus two times smaller for the highest resolution. The resolution of the precursor simulation is increased similarly, and the smaller scales of the turbulence are obtained by restarting the ABL simulation at the new resolution and converging it during $\simeq 25$ flow through times. The simulation with the resolution of 64 pts/D is also performed using the same precursor simulation, which is interpolated to the coarser resolution at the inflow plane. This ensures a valid comparison between the two simulations.

The mean forces distribution on the blades is depicted for both resolutions in Figure 16. The two distributions and their variances are very close. The thrust coefficient C_T is 0.687 for the simulation with 64 pts/D, and it slightly increases to 0.692 for 128 pts/D (+0.7%). Similarly, the power coefficient increases from 0.439 to 0.445 (+1.3%). The general shape of the distribution remains consistent between the two simulations, also near the tip, which suggests a sufficient discretization of the blade and of the wake.

The variation of the aerodynamic forces and of the structural root moment are also depicted in figure 17. The presented PSDs match perfectly until the E1 frequency. For higher frequencies, the loads predicted using 128 pts/D are higher. This is due to the additional unsteadiness induced by the smaller turbulent scales that are resolved up to a higher frequency when at high resolution, and to the smaller mollification size that reduces the smoothing induced by the integral velocity sampling. The magnitude of the PSD at these high frequencies is however much lower than that of the small frequencies, hence it is

https://doi.org/10.5194/wes-2024-19
Preprint. Discussion started: 19 February 2024

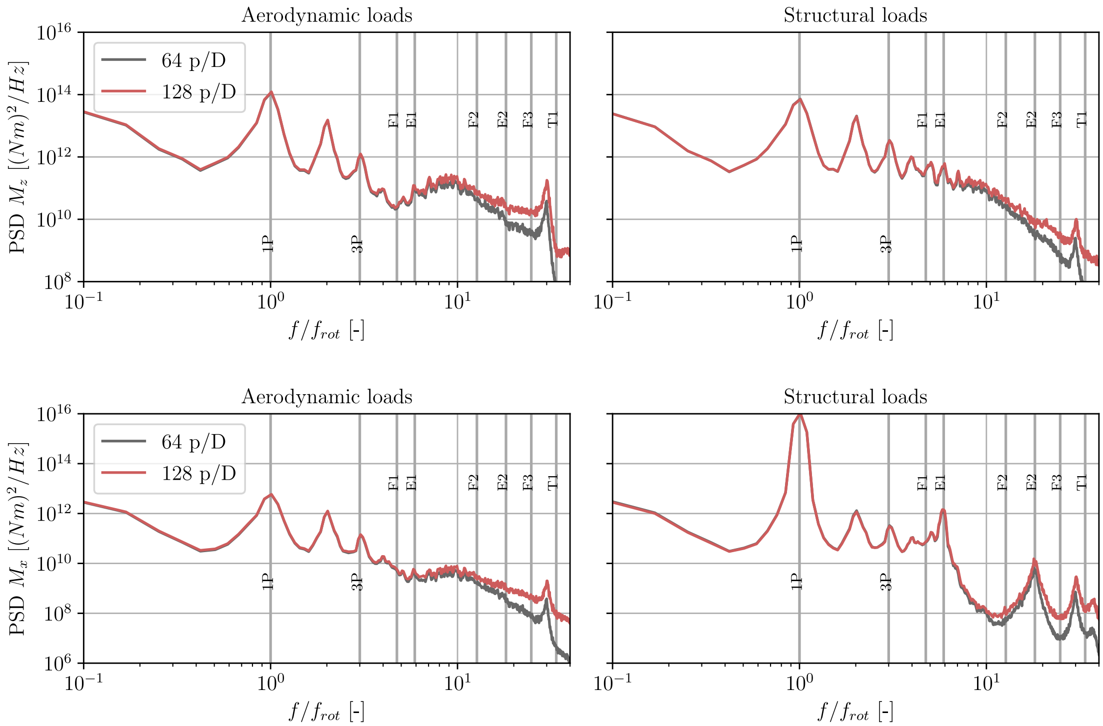

Figure 17. PSD of the blade root moment due to the flapwise forces (M_x, top) and edgewise forces (M_z, bottom). Left: PSD of the moment of the aerodynamic loads; right: PSD of the structural root moment. Comparison between two resolutions : 64 pts/D (gray) and 128 pts/D (red).

unlikely that this additional part of the spectrum significantly affects the fatigue of the blades and the wake. The peaks of the PSD located at the E2 and T1 frequencies are also obtained in both cases, indicating that the main components of the structural response are not significantly impacted by the resolution.

Figure 18 presents the instantaneous vorticity field behind the rotor with the two resolutions. We stress again that the turbulent inflows are at the same time for both resolutions. The same velocity field obtained at a resolution of 128 pts/D and at the same time t are used at the inflow of both simulations. The only difference is that the inflow is interpolated from 128 pts/D to 64 pts/D at the inflow plane of the coarser simulation. At higher resolution, the tip vortices have a smaller core size and hence a higher vorticity at their center (since they have essentially the same circulation in both cases). The hub vortices are also better resolved. The shed vortex sheet behind the outer part of the blade is also distinguishable. However, the larger structures of the wake are similar in both cases. This results in virtually identical velocity deficits as depicted in figure 19. The TKE has a higher value behind the hub and in the near tip regions, which results from the sharper mollification and the smaller scales captured by the simulation. However, this does not affect the mean velocity deficit.

https://doi.org/10.5194/wes-2024-19
Preprint. Discussion started: 19 February 2024

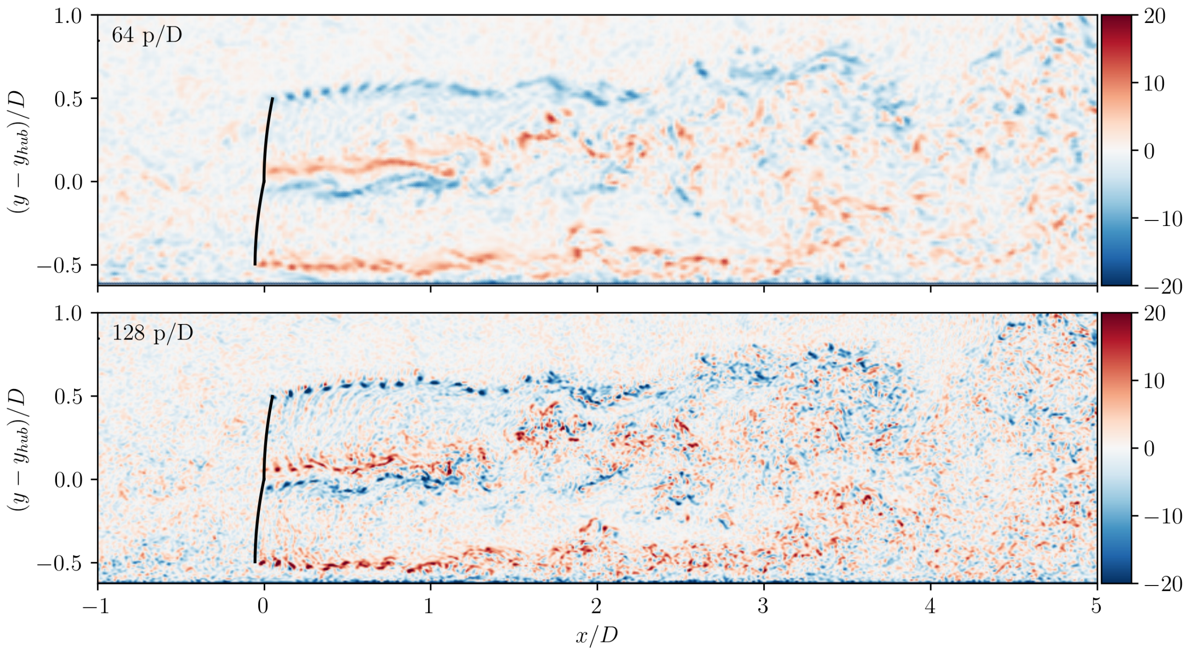

Figure 18. Snapshot of an instantaneous out-of-plane vorticity field ($\omega_z D/U_{hub}$) in the wake of the turbine for the 64 pts/D resolution (top) and the 128 pts/D resolution (bottom) cases. The inflow is identical for each case.

6 Conclusions

This work presented an investigation of the effect of the flexibility of the blades over the loads and the wake for the large IEA 15-MW reference wind turbine. An advanced flexible actuator line method (ALM), coupled to the non-linear structural solver *BeamDyn*, is used in large eddy simulation (LES) to compute the unsteady aerodynamic forces exerted by the turbulent inflow along each blade, and their influence over the flow. This methodology leverages the LES capabilities to simulate realistically the unsteadiness of the inflow and the wake produced by the turbine, so as to quantify the effect of the structural blade deformations on the loads and the wake.

The results obtained using the flexible actuator line method are first compared to those obtained using OpenFAST. In uniform flow, the free-vortex wake model of OpenFAST and the present flexible ALM predict very similar distributions for the forces, and which are slightly higher than those predicted using a BEM in the tangential direction. The effect of the deformation of the blades on the time-averaged loads is also predicted similarly by OLAF and the ALM. The magnitude of this effect is larger than that predicted by the BEM, which indicates that higher fidelity aerodynamic models are necessary to account for the effect of large displacements on the blade aerodynamics. Comparisons carried using a turbulent inflow without mean shear (generated using the Mann algorithm) show that the power spectral density (PSD) of the blade displacements are very similar for all three methods, which confirms that the flexible actuator line model is able to correctly capture the structural dynamics.

https://doi.org/10.5194/wes-2024-19
Preprint. Discussion started: 19 February 2024

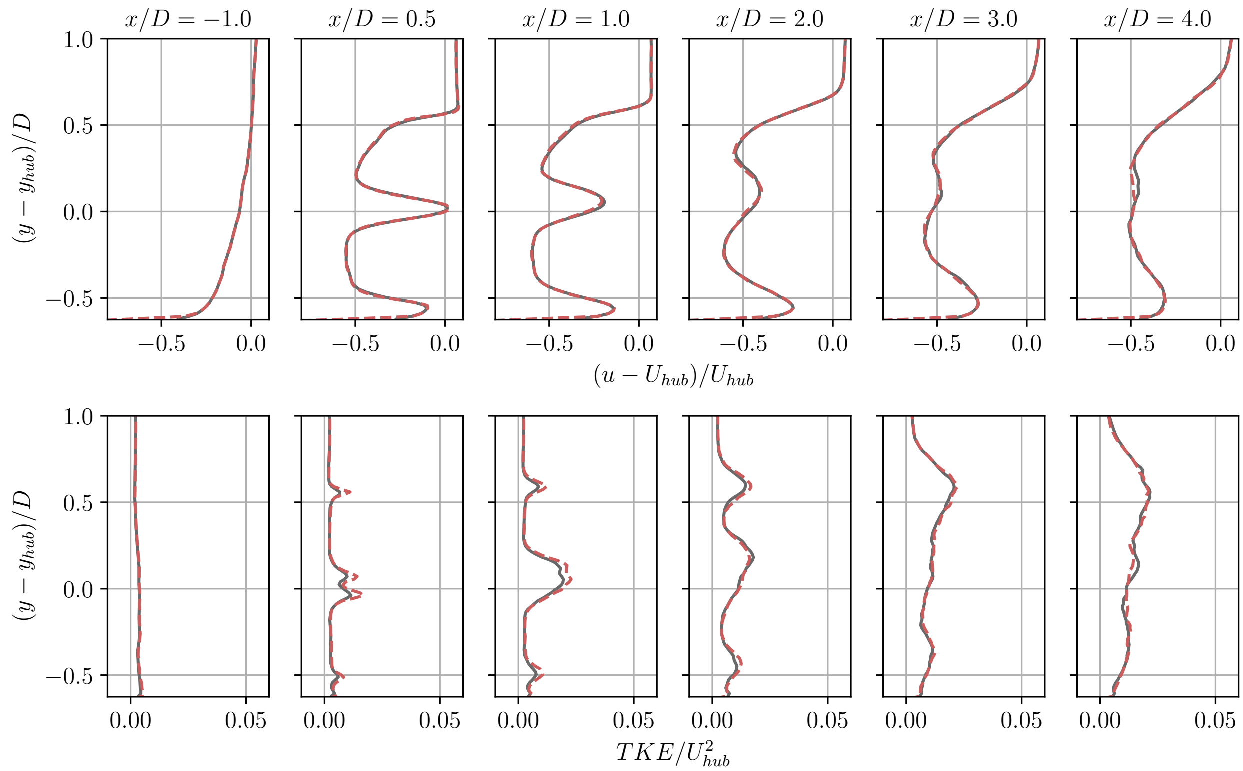

Figure 19. Profiles of mean velocity deficit (top) and turbulent kinetic energy (bottom) in the near wake of the turbine at various downstream locations. Comparison between the 64 pts/D (gray) and 128 pts/D (dashed red) resolutions.

The displacement and loads of the blades are then investigated in a turbulent atmospheric boundary layer (generated using a co-simulation). Significant flapwise and torsional displacements are observed, that importantly modify the aerodynamics of the blades. The resulting thrust coefficient decreases by 14% and the power coefficient by 10% compared to the rigid undeformed case. Including the mean deformation while keeping the rotor rigid allows to correctly recover the mean load distribution along the blade, which leads to thrust and power coefficients equivalent to those obtained using the flexible actuator line method. However, the variation of the loads during the blade rotation is different, especially close to the blade downwards position due to the high mean shear of the flow. Moreover, the aerodynamic loads and the structural response at the blade natural frequencies are noticeably affected by the flexibility. We also show that the variation of the angle of attack due to the flapwise blade velocity is significant, and of the same order of magnitude as that due to the blade torsion.

The wake behind the turbine is then considered. The results show that it is essential to include the mean deformation of the blade to obtain the correct mean velocity deficit and profile of turbulent kinetic energy. Once the mean deformation is added, the differences between the rigid deformed and the flexible cases are limited. In the near wake, the time-averaged velocity obtained in the flexible case is up to 4% slower at the bottom of the rotor swept area than in the rigid deformed case. The

https://doi.org/10.5194/wes-2024-19
Preprint. Discussion started: 19 February 2024

turbulent kinetic energy is slightly higher over the rotor area, which results from the unsteady variations of the loads and displacements. However, these changes do not affect significantly the global wake behavior.

Finally, the effect of the LES flow solver resolution over the wake is investigated by increasing the spatial discretization to 128 grid points per diameter. The mean load distribution is comparable to that obtained using the resolution with 64 grid points per diameter. The PSD of the root moment is also identical up to the first edgewise frequency. For the higher frequencies, a difference in magnitude is observed due to the higher frequency fluctuations captured by the LES (due to the twice higher cut-off wavenumber of the grid). A snapshot of the wake vorticty field shows tip vortices with a smaller core size and hence a higher vorticity at their center, and smaller turbulent scales in the flow. However, the time-averaged velocity deficits are largely similar between the two simulations. The TKE is higher behind the blade root and tip at high resolution, yet this does not impact the turbulent wake diffusion rate. As a result, it is unlikely that a higher resolution would significantly increase the impact of the unsteady displacements and load variations over the wake. It would however be necessary if the spectrum of the loads must be obtained at high frequencies.

The impact of the structural deformations over the loads and wake of a large 15 MW turbine is thus significant. These effects consist in a reduction of the thrust and power coefficients, a variation of the load distribution over the blade, and a modification of the spectrum of the blade root moments. These changes, in turn, substantially affect the near wake by altering the profiles of the velocity deficit and turbulent kinetic energy. In the relatively steady operating conditions considered in this paper (i.e., constant time-averaged wind velocity, turbulence intensity and rotation speed), the proper mean load distribution and wake behavior can be obtained using rigid blades but only when adjusting their geometry to incorporate their mean structural deformation. The latter was here obtained by time-averaging the structural deformation produced by our fully coupled unsteady simulations; but it could also be obtained in a preprocessing step, using alternative aeroelastic simulation tools. This then removes the need for the unsteady coupling of the structural solver and the actuator line of the LES solver, thereby slightly reducing the computational cost. However, the unsteady variations around the mean would still differ compared to those of the fully coupled simulation, resulting in a different spectrum of the loads. It is hence recommended to include the structural dynamics of the blades if the unsteady variation of the loads is of interest, particularly for blade structural integrity assessment, or to assess the benefits of load alleviation control methods.

Code and data availability. The LES flow solver BigFlow is not publicly available. The presented simulations results are available upon request.

Appendix A: Parallel implementation of the ALM and structural solver

The following appendix describes in more details the strategy employed for parallelizing the computations related to the ALM and the structural solver. A separate subcommunicator is defined for each wind turbine, which is split from the main communicator based on the turbine location. Any process containing a grid point closer to the hub than a distance D is

https://doi.org/10.5194/wes-2024-19
Preprint. Discussion started: 19 February 2024

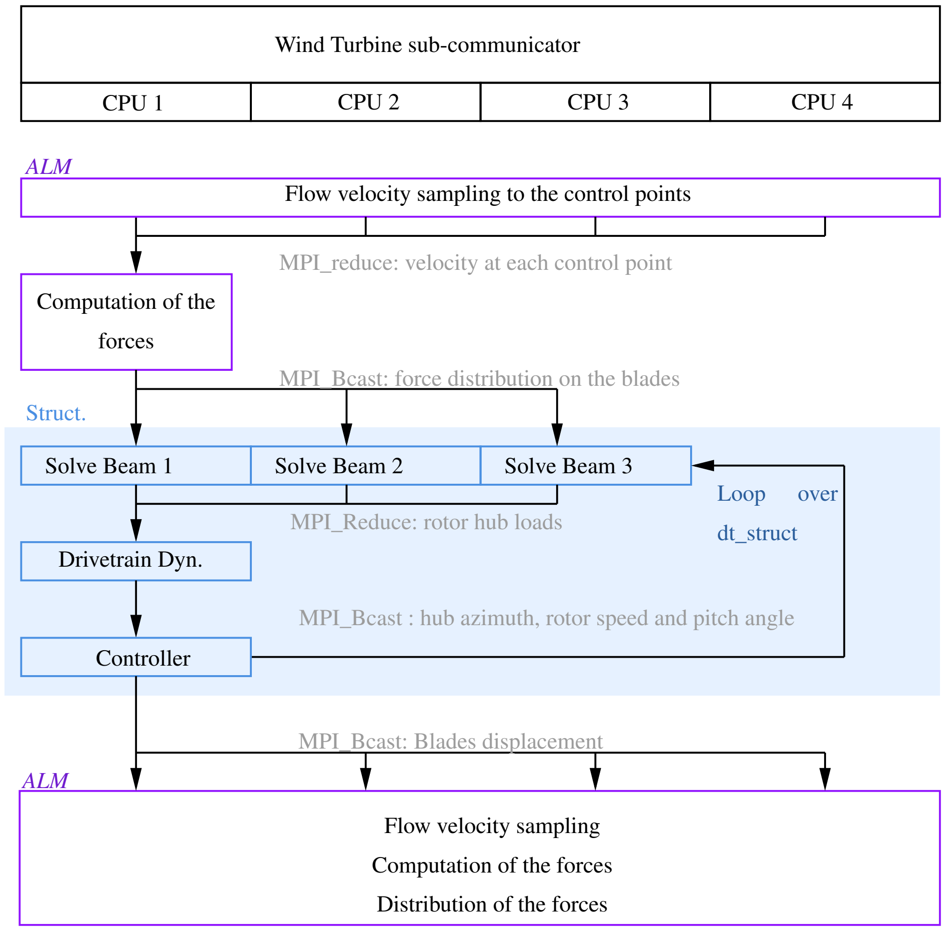

Figure A1. Schematic of the structural coupling.

https://doi.org/10.5194/wes-2024-19
Preprint. Discussion started: 19 February 2024

included in the turbine communicator. As the subcommunicators of each turbine generally comprise distinct set of processors, the tasks related to the ALM and the structural solver can be performed concurrently for each turbine. The different steps performed on the local set of processes are shown in Figure A1. The subcommunicator is first used to sample the velocity within a restricted region of the physical domain, thereby decreasing the communication overhead. The aerodynamic forces are computed on the root processor using the sampled velocities. Subsequently, the forces are broadcasted to the structural solver, which executes one instance of *BeamDyn* per blade on different processors. The time-integration of the blade dynamics is therefore performed in parallel, and the resulting root moments of each blade are sent to the root process. The latter computes the drivetrain dynamics and the controller commands at each structural sub-step. The beam solver only takes the hub azimuth and the pitch angle (and their time derivatives) as input and only needs to provide the forces and moments on the hub as output. Consequently, the overhead of the added communications required to solve the blades dynamics in parallel is largely overcomed by the benefits of the parallelization. After completion of the sub-steps, the blade displacements are broadcasted to all the processors of the subcommunicator to be used for the reevaluation of the forces and their distribution. The following parallelization allows to keep the computational cost of the ALM and of its coupling to *BeamDyn* reasonably low, and provide an efficient scaling in the case of multiple turbines.

Appendix B: Statistics of the simulated atmospheric boundary layer

This section presents the statistics of the neutral ABL that is used as inflow for the wind turbines. It is here obtained by simulating a turbulent half channel flow of height $H = 4\,D$; hence $H = 960$ m. The flow is driven using a pressure gradient $(-dp/dx)/\rho$=1.148e-04 $\mathrm{m\,s^{-2}}$ (with $\rho = 1.225\ \mathrm{kg\,m^{-3}}$ for air). The lateral boundary conditions are periodic. The upper boundary condition is a no-slip condition. At the ground, a wall model is used. The latter imposes the shear stress at the wall using the law of the wall for a rough wall,

$$u(y) = \frac{u_\tau}{\kappa} \log\left(\frac{y}{y_0}\right), \tag{B1}$$

with $\kappa = 0.385$ and $y_0 = 0.0016$ m. The computational domain is $8\,D \times 4\,D \times 4\,D$ with a resolution of 64 grid points per D. The time-step is set to $dt = 0.05$ s and the simulation is run for 584 convective times $t^* = tU_{\mathrm{hub}}/(8D)$ before it reaches convergence. The following statistics are then computed over $\simeq 100$ convective times.

The obtained profile of the mean streamwise velocity and of the turbulence intensity are shown in figure B1. The mean velocity profile indeed corresponds to a logarithmic profile with $u_\tau = 0.332\ \mathrm{m\,s^{-1}}$, and the turbulence intensity decreases linearly with height. The mean velocity of $10\ \mathrm{m\,s^{-1}}$ is obtained at the hub, as well as a TI of $\simeq 5\%$ when computed using the three velocity components. The auto-correlation functions of the streamwise velocity, $\rho^x_{u,u}$ and $\rho^z_{u,u}$ in the streamwise and lateral directions respectively, are also depicted in figure B2. These are used to compute the integral length scale in the streamwise and lateral directions, L^x_u and L^z_u, obtained by integration (Stanislawski et al., 2023):

$$L_u = \int_0^{\hat{\delta}} \langle \rho_{uu}(\delta) \rangle \, d\delta, \tag{B2}$$

https://doi.org/10.5194/wes-2024-19
Preprint. Discussion started: 19 February 2024

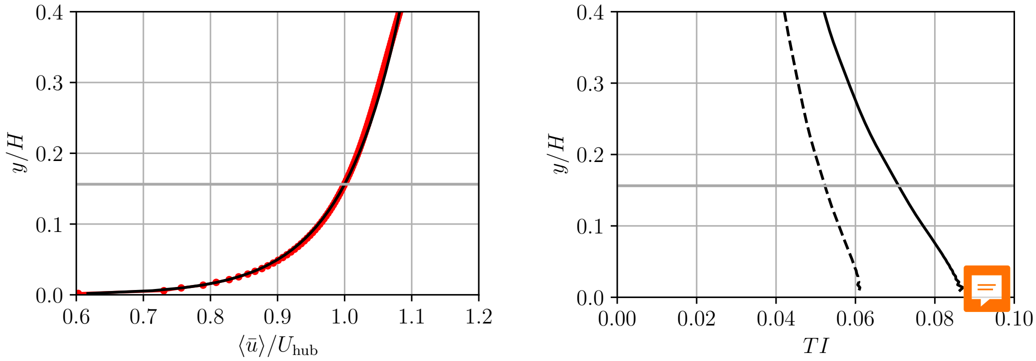

Figure B1. Left: profile of the obtained mean streamwise velocity (dotted red), and its comparison to a logarithmic profile (solid black). Right: profile of the turbulence intensity based on the streamwise velocity (solid) and on the three velocity components (dashed). The horizontal gray line indicates the hub height.

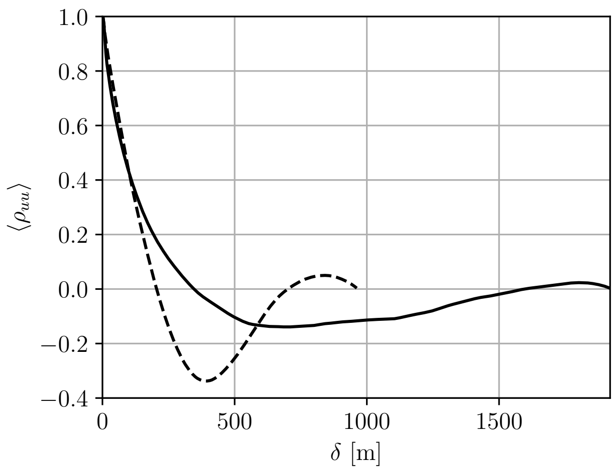

Figure B2. Auto-correlation functions of the streamwise velocity in the streamwise ($\langle\rho^x_{uu}\rangle$, solid) and lateral ($\langle\rho^z_{uu}\rangle$, dash) directions. The values are averaged over the horizontal plane at hub height

where $\hat{\delta}$ is the distance where the correlation function is smaller than 0.05. This leads to L^x_u = 106 m = 0.44D and L^z_u = 89.5 m = 0.37D.

https://doi.org/10.5194/wes-2024-19
Preprint. Discussion started: 19 February 2024

555 *Author contributions.* FT, PC and GW conceptualized this research and established the methodology. FT developed the software for the coupling, ran and post-processed the simulations, with the help of PC and GW for the investigation process. FT prepared the original draft with contribution from all authors, which was then reviewed by PC and GW. GW provided funding.

Competing interests. The authors report no conflict of interests

Acknowledgements. The authors would like to thank Dr. Matthieu Duponcheel and Dr. Maud Moens for their advices and help at multiple
560 stage of this research. The research funding was provided in the frame of the PhairywinD project funded by the Belgian Federal Government under the Energy Transition Fund. Computational resources have been provided by the Consortium des Équipements de Calcul Intensif (CÉCI), funded by the Fonds de la Recherche Scientifique de Belgique (F.R.S.-FNRS) under Grant No. 2.5020.11 and by the Walloon Region. The present research also benefited from computational resources made available on Lucia, the Tier-1 supercomputer of the Walloon Region, infrastructure funded by the Walloon Region under the grant agreement n°1910247.